Accepted Manuscript

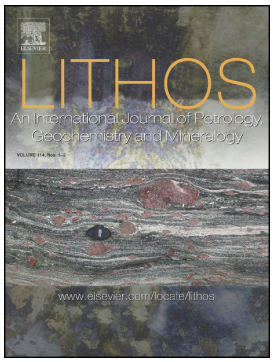

Can we extract ultrahigh-temperature conditions from Fe-rich metapelites? An example from the Khondalite Belt, North China Craton

Xianwei Li, Richard William White, Chunjing Wei

PII: S0024-4937(19)30052-0
DOI: https://doi.org/10.1016/j.lithos.2019.01.032
Reference: LITHOS 4962

To appear in: *LITHOS*

Received date: 3 September 2018
Accepted date: 24 January 2019

Please cite this article as: X. Li, R.W. White and C. Wei, Can we extract ultrahigh-temperature conditions from Fe-rich metapelites? An example from the Khondalite Belt, North China Craton, LITHOS, https://doi.org/10.1016/j.lithos.2019.01.032

Can we extract ultrahigh-temperature conditions from Fe-rich metapelites? An example from the Khondalite Belt, North China Craton

Xianwei Li [a,b,*], Richard William White [b], Chunjing Wei [a]

[a] MOE Key Laboratory of Orogenic Belts and Crustal Evolution, School of Earth and Space Sciences, Peking University, Beijing, China

[b] School of Earth and Environmental Sciences, University of St Andrews, Scotland, United Kingdom

[*] Corresponding author.

Email address: lixwchn@pku.edu.cn (X. Li).

ABSTRACT

In this study, garnet–sillimanite gneisses at Hongshaba in the eastern segment of the Khondalite Belt, North China Craton (NCC) are interpreted to have experienced ultrahigh-temperature (UHT) metamorphism (980–1040°C) followed by post-T_{max} cooling at pressures of 8–9 kbar to the solidus (810–830°C), consistent with rare sapphirine-bearing assemblages in surrounding regions. This interpretation is mainly based on the combination of *P*–*T* fields and garnet X_{gr} (=Ca/(Ca+Mg+Fe^{2+})) isopleths on the pseudosection of three garnet–sillimanite gneiss samples. Spinel tends to be enclosed in the outer margins of garnet, commonly closely associated with quartz. We interpret this to reflect the partial break down of garnet along the prograde path during heating with decompression followed by new garnet growth during cooling along an overall clockwise *P*–*T* evolution. Although Fe-rich UHT metapelites tend to contain neither diagnostic mineral assemblages nor orthopyroxene from which to extract *T* via Al-in-orthopyroxene thermometry, isopleths of Ca in garnet may aid in retrieving UHT conditions from these compositions. This is attributed to Ca diffusion in garnet being much slower than Fe and Mg diffusion, leading to little change in Ca contents during post-T_{max} cooling. LA-ICP-MS U–Pb dating of metamorphic zircon in one garnet–sillimanite gneiss sample yields a mean $^{207}Pb/^{206}Pb$ age of *ca.* 1.91 Ga, which is interpreted to record the timing of cooling of the UHT rocks to the solidus. This UHT metamorphism is interpreted to have been generated by mantle-derived magma during a tectonic extension from *ca.* 1.95 to 1.92 Ga within a post-orogenic setting.

Keywords:

Khondalite Belt; North China Craton; phase equilibrium modelling; ultrahigh-temperature metamorphism; zircon geochronology

1. Introduction

Ultrahigh-temperature (UHT) metamorphism is the most extreme type of thermally-driven regional-scale crustal metamorphism at temperatures exceeding 900°C (Harley, 1998). Evidence for UHT conditions is generally retrieved from mineral assemblages formed in Mg-rich metapelites, such as sapphirine–quartz- or orthopyroxene–sillimanite-bearing assemblages (e.g. Harley, 2008; Kelsey, 2008), which are considered to be a diagnostic indicator of temperatures above 900°C (e.g. Harley, 1998; Hensen and Green, 1973), albeit with some important caveats involving the oxidation state of the rock (Taylor-Jones and Powell, 2010) and the presence of melt and K-feldspar (Diener et al., 2008). Furthermore, the Al_2O_3 content of orthopyroxene in metapelites can additionally be used to infer UHT conditions (e.g. Harley and Motoyoshi, 2000; Kelsey et al., 2003). However, Mg-rich metapelites are relatively rare in most granulite-facies terrains, being subordinate to more common aluminous Fe-rich metapelite. Unfortunately, the latter metapelites tend to contain neither diagnostic UHT assemblages nor orthopyroxene and the common garnet–sillimanite-bearing assemblage is stable over a large *P–T* field within pseudosections (e.g. White et al., 2002), which makes it difficult to retrieve UHT conditions from such rocks. In this case, precise T_{max} conditions tend not to be easily obtained through phase equilibrium modelling and other methods, such as two-feldspar thermometry (e.g. Fuhrman and Lindsley, 1988) and trace element thermometry (e.g. Ferry and Watson, 2007; Tomkins et al., 2007), must be applied. Nevertheless, as some cations such as Ca^{2+} in garnet and plagioclase within Fe-rich metapelites shows similar low diffusion rate as Al^{3+} in orthopyroxene within Mg-rich metapelites (e.g. Chakraborty and Ganguly, 1992; Hollis et al., 2006; Spear and

Florence, 1992), there is still the potential to extract more detailed *P–T* information from Fe-rich metapelites using selected mineral composition isopleths from phase equilibrium modelling. The compositional limitations of diagnostic UHT assemblages and the relative rarity of UHT-sensitive compositions create a significant challenge in identifying metamorphism under UHT conditions and constraining the areal extent of such metamorphism. This has implications for the origin and tectonic setting of any UHT metamorphic terrain. For example, small localized areas of UHT metamorphism in larger non-UHT regions require only local thermal perturbations, which may be of little tectonic significance whereas extensive terrain-scale UHT conditions require significant thermal perturbations on a large, tectonically-significant, scale (e.g. Clark et al., 2011).

This issue is well illustrated in the eastern sector of the Paleoproterozoic Khondalite Belt, which is part of the Western Block of the North China Craton (NCC) (Fig. 1), where both 'normal' (garnet–sillimanite) and UHT (sapphirine–quartz or orthopyroxene–sillimanite) metapelitic granulites occur. The 'normal' granulites are widespread (Fig. 1c). They are Fe-rich and characterized by garnet–sillimanite-bearing assemblages, which have been interpreted to record peak temperatures of ~850°C along clockwise *P–T* paths (e.g. Cai et al., 2014; Lu and Jin, 1993; Wang et al., 2011). The UHT granulites only crop out in a few localities (Fig. 1c). They are also rich in total Fe and commonly contain sapphirine and orthopyroxene but formed under oxidized conditions such that they have low proportions of Fe^{2+} (sapphirine-bearing granulites). The sapphirine-bearing rocks commonly occur with spinel-bearing garnet–sillimanite gneisses which formed under somewhat more reduced conditions. Overall, these rocks are interpreted to record temperatures above 950°C along clockwise *P–T* paths (Li and Wei, 2016, 2018; Yang

et al., 2014) or counterclockwise *P–T* paths (Liu et al., 2008, 2012; Santosh et al., 2007a, 2009a, 2012; Shimizu et al., 2013; Zhang et al., 2012). It still remains unclear whether there are more garnet–sillimanite gneisses in this region recording UHT conditions and whether the evolution of the UHT rocks is clockwise or counterclockwise.

In this study, we investigate the garnet–sillimanite gneisses at Hongshaba within the eastern Khondalite Belt, NCC (Fig. 1c). The goal is to determine the metamorphic *P–T* conditions of these Fe-rich metapelites using phase equilibrium modelling and determine the ability of such rocks to record meaningful UHT conditions. Additionally, we constrain the timing of the metamorphism via LA-ICP-MS zircon U–Pb dating.

2. Geological setting

The North China Craton is divided into the Archean to Paleoproterozoic Eastern and Western Blocks and three Paleoproterozoic orogenic belts, namely the Trans-North China Orogen, the Khondalite Belt and the Jiao–Liao–Ji Belt (e.g. Zhao et al., 2005). The Western Block is traditionally interpreted to have formed at *ca*. 1.95 Ga when the Yinshan and Ordos Blocks collided along the Khondalite Belt and the North China Craton is believed to have been amalgamated at *ca*. 1.85 Ga when the Western and Eastern Blocks collided along the Trans-North China Orogen (Fig. 1a; e.g. Zhao et al., 1998, 2005, 2012). Nevertheless, recent studies show that the collision between the Western and Eastern Blocks may alternatively have occurred at *ca.* 1.95 Ga (Qian and Wei, 2016; Qian et al., 2013, 2015) and the large number of zircon ages of *ca.* 1.85 Ga obtained from granulite facies rocks could instead reflect the cooling and exhumation of these high-grade terranes (Wei et al., 2014; Zhang et al., 2013).

The E–W-striking Paleoproterozoic Khondalite Belt in the Western Block extends from Jining in the east, through Daqingshan–Wulashan, to Qianlishan–Helanshan in the west (Fig. 1b). The lithologies within the Khondalite Belt are mainly garnet–sillimanite/kyanite gneisses, quartzo-feldspathic gneisses, garnet quartzites, calc-silicate rocks, graphite-bearing metapelites and marbles associated with S-type granites, charnockites, TTG gneisses, mafic granulites and amphibolites (Condie et al., 1992; Lu et al., 1992). The protoliths of the metasedimentary rocks are generally interpreted to represent stable continental margin deposits (e.g. Lu and Jin, 1993; Lu et al., 1992, 1996; Zhao et al., 2005), though others believe that they could have been deposited in cratonic basins (e.g. Condie et al., 1992; Zhai and Peng, 2007) or active continental margins (e.g. Dan et al., 2012). Their detrital zircons yield ages of 2.9–2.0 Ga and the timing of the deposition is constrained to be after *ca*. 2.0 Ga (e.g. Dan et al., 2012; Dong et al., 2007, 2013; Wan et al., 2006). These supracrustal rocks are believed to record a complex history of high-grade metamorphism from >1.95 to *ca*. 1.84 Ga (e.g. Dong et al., 2007, 2013; Li et al., 2011; Wan et al., 2006; Yin, 2010). Among the metasedimentary rocks, medium-pressure (MP) pelitic granulites characterized by the paragenesis garnet–sillimanite are dominant (e.g. Cai et al., 2014) while high-pressure (HP) pelitic granulites characterized by the paragenesis garnet–kyanite are mainly reported from Qianlishan–Helanshan (e.g. Yin, 2010; Zhou et al., 2010). Furthermore, small amounts of garnet–sillimanite gneisses containing kyanite inclusions within garnet grains are identified from Jining (e.g. Wang et al., 2011; Wu et al., 2017).

The Jining region in the eastern section of the Khondalite belt (Fig. 1b) is dominated by ‘normal’ pelitic granulites characterized by the paragenesis garnet–sillimanite (e.g. Cai et al., 2014; Lu and Jin, 1993; Wang et al., 2011) with

UHT pelitic granulites present only in a few localities (Fig. 1c), as mentioned above. Only the UHT metapelites at Tuguiwula and Xuwujia (e.g. Santosh et al., 2007a, 2009a) contain the diagnostic UHT assemblage sapphirine–quartz, whereas the UHT rocks in other localities contain spinel occurring as inclusions within garnet/sillimanite (e.g. Liu et al., 2012; Yang et al., 2014; Zhang et al., 2012).

Regarding zircon dating, within the Jining region, metamorphic zircons related to the 'normal' granulites yield ages of 1.98–1.96 Ga (Li et al., 2011), *ca*. 1.91 Ga (Cai et al., 2014) and 1.89–1.84 Ga (Jiao et al., 2013; Li et al., 2011; Wan et al., 2006), while metamorphic zircons in the UHT granulites yield ages of *ca*. 1.92 Ga (Li and Wei, 2018; Santosh et al., 2007b, 2009b, 2013) and *ca.* 1.88 Ga (Yang et al., 2014). Furthermore, S-type granites show crystallization ages of 1.92–1.90 Ga (Zhong et al., 2007) and gabbronorites show crystallization ages of *ca*. 1.93 Ga (Peng et al., 2010).

Hongshaba lies 25 km to the north of Liangcheng (Fig. 1c) where both garnet–sillimanite gneisses (Fig. 2a–c) and garnet-bearing S-type granites occur (Fig. 2d). Regarding the appearance of garnet–sillimanite gneisses, they can range from leucocratic (Fig. 2a) to melanocratic varieties (biotite- and sillimanite-bearing; Fig. 2b). Garnet-bearing leucosomes occur within the garnet–sillimanite gneisses (Fig. 2c), suggesting that partial melting occurred during the high-grade metamorphism.

3. Petrography and mineral compositions

Three garnet–sillimanite gneiss samples (J1448, J1542 and J1544) were collected from Hongshaba (Fig. 1c). Mineral compositions of these samples were determined using a JXA-8100 microprobe at Peking University under operating conditions of 15 kV acceleration voltage and a 1.0×10^{-8} A current with a beam diameter of 2 μm. Natural and synthetic minerals from the SPI Company were used for standardization.

The analysis results are presented in Tables 1 and 2. Photomicrographs are shown in Fig. 3.

All three samples of garnet–sillimanite gneiss in this study are similar with respect to their mineral assemblages and microstructures. They contain garnet, sillimanite, K-feldspar, quartz with minor amounts of spinel, biotite and plagioclase. Accessory minerals are predominantly rutile (matrix) and ilmenite (inclusion and matrix) in J1448 and J1544, whereas in J1542, rutile (matrix) is the predominant accessory mineral.

Garnet commonly occurs as anhedral grains (2–8 mm across) and inclusions in garnet are predominantly biotite and quartz (Fig. 3a,d,g). Additionally, in J1448, spinel is also included in garnet (Fig. 3a,b). Garnet in J1448 contains 52–56% almandine (Alm) ($Fe^{2+}/(Fe^{2+}+Mg+Ca+Mn)$, defined accordingly for other components), 40–43% pyrope (Pyr), 3.5–4.0% grossular (Grs) and 0.7–0.9% spessartine (Sps). Garnet in J1542 and J1544 has similar composition of $Alm_{56–61}Pyr_{35–41}Grs_{2.5–2.7}Sps_{0.7–1.0}$ and $Alm_{58–61}Pyr_{36–39}Grs_{2.4–2.7}Sps_{0.9–1.3}$ respectively. There is no significant difference in composition between the core and the rim of a single garnet grain.

Sillimanite generally occurs as elongate prismatic crystals (0.2–1.6 mm) in the matrix. Some sillimanite grains include spinel (Fig. 3a,b,e,g).

Biotite mainly occurs as irregular flakes (0.1–1.5 mm) in the matrix (Fig. 3c,e,f,h) and minor amounts of biotite occur within garnet grains (Fig. 3a,d,g). In all three samples, matrix-type biotite shows similar composition with X_{Mg} ($=Mg/(Mg+Fe^{2+})$) of 0.67–0.75 and TiO_2 of 3.66–5.33 wt% (Ti (pfu) = 0.20–0.29) (Fig. 4). Biotite inclusions show similar X_{Mg} of 0.77–0.84, but also show a wide TiO_2 range of 3.70–6.70 wt% (Ti (pfu) = 0.20–0.37) (Fig. 4).

Spinel commonly occurs as grains (0.1–1.1 mm) enclosed in the outer margins of garnet (Fig. 3a,b), in sillimanite (Fig. 3a,b) or in plagioclase within K-feldspar (Fig. 3b) in J1448, and enclosed in sillimanite in J1542 (Fig. 3e) and J1544 (Fig. 3g). Spinel and quartz tend to be separated by thin rims of garnet and/or sillimanite (Fig. 3a,b,e,g), thus spinel and quartz are inferred to have been in equilibrium near the peak conditions of metamorphism before being separated by garnet or sillimanite. Spinel shows X_{Mg} of 0.43–0.52 and ZnO of 2.21–3.04 wt% in J1448, X_{Mg} of 0.40–0.42 and ZnO of 5.10–6.88 wt% in J1542, and X_{Mg} of 0.35–0.36 and ZnO of 3.79–4.17 wt% in J1544.

K-feldspar mainly occurs as medium-to-coarse-grained crystals (0.5–1.9 mm) in the matrix. In all three samples, K-feldspar shows similar composition with X_{Or} (=K/(Ca+Na+K)) of 0.77–0.92. Plagioclase commonly occurs as medium-grained crystals (0.1–1.0 mm) in the matrix (Fig. 3f,h). It shows X_{An} (=Ca/(Ca+Na+K)) of 0.37–0.38 in J1448 and 0.26–0.28 in J1542 and J1544. Additionally, in J1448, plagioclase also occurs as moats around spinel within K-feldspar (Fig. 3b) with X_{An} of 0.41–0.43. Quartz mainly occurs as grains of 0.2–1.5 mm in the matrix.

Based on the observations above, the peak assemblage of J1448 and J1544 is interpreted to contain g–sill–sp–ksp–q–ilm±pl±ru with melt, and their solidus assemblage is interpreted to contain g–bi–sill–ksp–pl–q–ru–ilm. Furthermore, the peak assemblage of J1542 is interpreted to contain g–sill–sp–ksp–q±pl±ru±ilm with melt, and the solidus assemblage is interpreted to contain g–bi–sill–ksp–pl–q–ru.

4. Bulk-rock compositions

The bulk-rock compositions of the three garnet–sillimanite gneiss samples (J1448, J1542 and J1544) were determined by ICP-OES analysis at China University of

Geoscience (Beijing) and the results are shown in Table 3. The Fe^{3+}/Fe^{T} values were determined by Fe^{2+} titration. These three samples have similar compositions. They are all rich in SiO_2 (61.81–65.05 wt%), Al_2O_3 (16.11–19.39 wt%) and K_2O (2.88–3.42 wt%), poor in CaO (0.60–0.99 wt%) with a molar $Mg/(Mg+Fe^{T})$ of 0.44–0.46, indicating a Fe-rich pelitic protolith. Furthermore, the low measured Fe^{3+}/Fe^{T} values (0.01–0.04) suggest that these rocks might once equilibrated at rather reduced conditions.

5. Phase equilibrium modelling

Phase equilibria were modelled for the three garnet–sillimanite gneiss samples (J1448, J1542 and J1544) in the NCKFMASHTO (Na_2O–CaO–K_2O–FeO–MgO–Al_2O_3–SiO_2 –H_2O–TiO_2–Fe_2O_3) system. This system provides a realistic approximation to the composition of the samples within which the effects of melt and Fe^{3+} may be assessed (e.g. White et al., 2007). Calculations were performed using THERMOCALC (Powell and Holland, 1988) with the internally consistent thermodynamic dataset, ds62, of Holland and Powell (2011). The *a–x* models of White et al. (2014a) were used for melt, garnet, biotite, cordierite and orthopyroxene, Holland and Powell (2003) for plagioclase and K-feldspar, White et al. (2000) for ilmenite–hematite and White et al. (2002) for spinel–magnetite. The bulk-rock compositions obtained by ICP-OES analysis were normalized in the NCKFMASHTO system (Table 4). The H_2O contents were adjusted using T–M_{H2O} diagrams to ensure that the final phase assemblages were stable just above the solidus (e.g. Korhonen et al., 2011, 2012; White et al., 2004). The O contents were determined by Fe^{2+} titration.

5.1. Sample J1448

The *P–T* pseudosection for sample J1448 was calculated with quartz in excess over the *P–T* window of 700–1100°C/4–12 kbar (Fig. 5a). The fluid-absent solidus occurs at *T* of 810–840°C above 6 kbar. Mineral composition isopleths of X_{gr} (=Ca/(Ca+Mg+Fe^{2+})) and X_{py} (=Mg/(Ca+Mg+Fe^{2+})) in garnet and X_{An} in plagioclase are plotted on the pseudosection.

The inferred peak assemblage g–sill–sp–ksp–q–ilm–liq±pl±ru of sample J1448 can only correspond to a narrow band (g–sill–sp–ksp–pl–q–ilm–liq) at *T* >980°C and *P* >6 kbar, highlighted in Fig. 5a and shown in detail in Fig. 5b. However, this *P–T* field may not reflect the peak *P–T* conditions as the measured spinels contain appreciable ZnO (Table 1) which is not considered in the model system. The stability of spinel in the rocks may thus extend to lower temperatures and higher pressures by at least 50°C and 1 kbar, based on the measured ZnO contents in the spinel in the rocks (e.g. Nichols et al., 1992).

If spinel is ignored, the inferred peak assemblage g–sill–sp–ksp–q–ilm–liq±pl±ru corresponds to the g–sill–ksp–pl–q–ilm–liq±ru fields in Fig. 5a. These fields additionally match the measured X_{gr} (0.035–0.040) contents in garnet which yield *P–T* estimates of >860°C/ >7 kbar. The measured X_{py} (0.40–0.43) in garnet and X_{An} (0.37–0.43) in plagioclase occur in biotite-bearing field and indicate somewhat lower *P–T* conditions of *T* <850°C and *P* = 7–9 kbar around the solidus. At a pressure of 8 kbar, the predicted melt modes are 0.07 at 900°C and 0.16 at 1000°C.

Mineral mode isopleths of garnet, sillimanite and spinel are also plotted on the pseudosection (Fig. 5a,b). Within the biotite- and spinel-absent fields (g–sill–ksp–pl–q–liq±ru±ilm), the modes of garnet and sillimanite slightly decrease with increasing temperature. Where spinel appears (g–sill–sp–ksp–pl–q–ilm–liq), garnet and sillimanite modes decrease significantly over a fairly narrow field with

increasing temperature (Fig. 5b). Although, the exact *P–T* conditions of this spinel-bearing field are uncertain due to the presence of ZnO in the rock, it is likely that the relative modal changes across it are approximately correct. This means that initial post-peak cooling at a pressure of ~8 kbar will lead to a considerable increase in the modes of garnet and sillimanite at the expense of spinel, consistent with the observation of spinel enclosed in garnet/sillimanite (Fig. 3a,b). Further cooling may cause the appearance of biotite at ~860°C above the solidus, which eventually gives the solidus assemblage g–bi–sill–ksp–pl–q–ru–ilm.

5.2. Sample J1542

The *P–T* pseudosection for sample J1542 was calculated with quartz in excess over the *P–T* window of 700–1100°C/4–12 kbar (Fig. 6a). The fluid-absent solidus occurs at *T* of 790–820°C above 6 kbar.

The inferred peak assemblage g–sill–sp–ksp–q–liq±pl±ru±ilm of sample J1542 can only correspond to a narrow band (g–sill–sp–ksp–q–ilm–liq±pl) at high *T* >990°C and *P* >6 kbar in Fig. 6a. Similar to the discussion for sample J1448 above, this *P–T* field may not reflect the peak *P–T* conditions as the measured spinels contain an appreciable ZnO content. In this case, the inferred peak assemblage may correspond to the g–sill–ksp–q–liq±pl±ru±ilm fields in Fig. 6a. These fields match the measured X_{gr} (0.025–0.027) contents in garnet which yield *P–T* estimates of >890°C/ >7 kbar. The measured X_{py} (0.35–0.41) in garnet and X_{An} (0.26–0.28) in plagioclase occur in biotite-bearing field and indicate somewhat lower *P–T* conditions of *T* <830°C and *P* = 7–9 kbar around the solidus. At a pressure of 8 kbar, the predicted melt modes are 0.10 at 900°C and 0.21 at 1000°C.

The topology of the mineral mode isopleths of garnet, sillimanite and spinel are

similar to those for sample J1448 (Fig. 6a,b). Initial post-peak cooling at a pressure of ~8 kbar will lead to an increase in the modes of garnet and sillimanite at the expense of spinel, consistent with the observation that spinel is included in sillimanite (Fig. 3e). Further cooling may cause the appearance of biotite at ~850°C above the solidus, which eventually gives the solidus assemblage g–bi–sill–ksp–pl–q–ru.

5.3. Sample J1544

The *P–T* pseudosection for sample J1544 was calculated with quartz in excess over the *P–T* window of 700–1100°C/4–12 kbar (Fig. 7a). The fluid-absent solidus occurs at *T* of 800–820°C above 6 kbar.

The inferred peak assemblage g–sill–sp–ksp–q–ilm–liq±pl±ru of sample J1544 can only correspond to a narrow band (g–sill–sp–ksp–pl–q–ilm–liq) at high *T* >970°C and *P* >6 kbar in Fig. 7a. Similar to the discussion for samples J1448 and J1542 above, this *P–T* field may not reflect the peak *P–T* conditions. In this case, the inferred peak assemblage may correspond to the g–sill–ksp–pl–q–ilm–liq±ru fields in Fig. 7a. These fields roughly match the measured X_{gr} (0.024–0.027) contents in garnet which yield *P–T* estimates of >840°C/ >7 kbar. The measured X_{py} (0.36–0.39) in garnet and X_{An} (0.26–0.28) in plagioclase occur in biotite-bearing field and indicate somewhat lower *P–T* conditions of *T* <840°C and *P* = 7–9 kbar around the solidus. At a pressure of 8 kbar, the predicted melt modes are 0.08 at 900°C and 0.16 at 1000°C.

The topology of the mineral mode isopleths of garnet, sillimanite and spinel are similar to those for samples J1448 and J1542 (Fig. 7a,b). Initial post-peak cooling at a pressure of ~8 kbar will lead to an increase in the modes of garnet and sillimanite at the expense of spinel, consistent with the observation that spinel is included in sillimanite (Fig. 3g). Further cooling may cause the appearance of biotite at ~840°C

above the solidus, which eventually gives the solidus assemblage g–bi–sill–ksp–pl–q–ru–ilm.

6. Zircon geochronology and Ti-in-zircon thermometry

Garnet–sillimanite gneiss sample J1448 was selected for zircon dating. Zircon grains were separated by conventional heavy liquid and magnetic separation followed by hand-picking under a binocular microscope. Selected grains were mounted in epoxy resin, polished down to expose the grain center, photographed in transmitted and reflected light, and imaged using cathodoluminescence (CL). CL imaging was carried out at Peking University on a FEI PHILIPS XL30 SFEG SEM with 2-min scanning time at conditions of 15 kV and 120 μA. The zircon U–Pb dating and trace element analyses were performed synchronously using LA-ICP-MS at the Key Laboratory of Orogenic Belts and Crustal Evolution, Ministry of Education, Peking University. Zircon 91500 was used as the standard and the standard silicate glass NIST was used to optimize the machine (Wiedenbeck et al., 1995, 2004). U–Pb isotopic compositions and trace element concentrations were calculated using GLITTER 4.4 (Van Achterbergh et al., 2001) and calibrated using ^{29}Si as an internal calibrant and NIST 610 as an external standard. The age calculations and plotting of Concordia diagrams used ISOPLOT 3.0 (Ludwig, 2003). Analyses described as concordant refer to those with <10% discordance. Apparent zircon crystallization temperatures were calculated using the Ferry and Watson (2007) calibration of the Ti-in-zircon thermometer.

Zircon grains in sample J1448 are mostly round to weakly elongate in shape. They are mostly structureless in CL images (Fig. 8), suggesting that they were formed during high-grade metamorphism (e.g Corfu et al., 2003). Several zircon grains exhibit separate cores and rims (Fig. 8); the cores are commonly structureless and the

rims are too narrow to analyze. Thirty-five analyses were made on thirty-five grains; all of them are concordant (see Fig. 9 and Table 5). They yield a spread of $^{207}Pb/^{206}Pb$ ages from 1944 ± 20 to 1870 ± 17 Ma, with a mean age of 1910 ± 6 Ma (MSWD = 1.2, n = 35). Th/U ratios are 0.17–2.17, which are higher than those typically attributed to metamorphic zircons (e.g. Vavra et al., 1996) and they may reflect the presence of melt (e.g. Wan et al., 2006). The measured Ti concentrations correspond to apparent temperatures of 758–878°C with an average value of 838 ± 27°C (aTiO$_2$ = 1, aSiO$_2$ = 1; Ferry and Watson, 2007). The aTiO$_2$ and aSiO$_2$ values are based on the presence of both rutile and quartz.

7. Discussion and conclusion

7.1. Evolution of the Paleoproterozoic metamorphism

Based on the petrographic characteristics and on the calculated phase equilibrium of the garnet–sillimanite gneiss samples at Hongshaba in the eastern Khondalite Belt, NCC, UHT metamorphism can be infered with a post-T_{max} cooling-dominated path, consistent with rare sapphirine-bearing assemblages in surrounding areas such as Tuguiwula and Xuwujia (Fig. 1c; e.g. Santosh et al., 2007a, 2009a).

7.1.1. Peak P–T conditions

The modelling results of our samples, using a combination of *P–T* fields and garnet X_{gr} isopleths are consistent with peak *P–T* conditions of the Paleoproterozoic metamorphism in excess of 900°C and likely up to to 980–1040°C at 8–9 kbar (Fig. 10). Although the spinel-bearing fields suggest lower *P* and higher *T* conditions (Fig. 10), the presence of significant ZnO in spinel (Tables 1 and 2) can extend the stability field of this mineral to higher *P* and lower *T* (closer to the peak *P–T* conditions

derived from the X_{gr} isopleths), thus making the use of the reconstructed spinel-bearing assemblages to constrain the peak conditions potentially unreliable. Furthermore, although spinel is ignored, the position of garnet X_{gr} isopleth will not move too much as spinel does not contain appreciable Ca^{2+} and is not likely to largely affect the mode of garnet. This is because in a ZnO-present system, spinel modes will likely remain low where spinel is stabilized by addition of small quantities of ZnO in the bulk-rock composition. Thus we expect the effect of ZnO on spinel to be analogous with the effect of MnO on garnet where garnet modes remain low until garnet would become stable in the MnO-free subsystems (White et al., 2014b). Taking Fig. 5 as an example, the predicted spinel modes at lower *P* in a ZnO-absent system (~7%) would be much higher than the predicted spinel modes at higher *P* in a ZnO-present system and the latter ones could be smaller than 2%, consistent with the observed minor amounts of spinel in the sample. In addition, regarding the melt volumes at peak conditions, the predicted melt modes are 0.16, 0.21 and 0.16 for samples J1448, J1542 and J1544 respectively at 1000°C and 8kbar. Though these modes may be a bit high with regard to the melt connectivity threshold (Rosenberg and Handy, 2005), they have little influence on the peak conditions predicted by pseudosection.

The inferred peak conditions in this study are consistent with the results from previous studies in the Jining region (e.g. Jiao and Guo, 2011; Li and Wei, 2016, 2018; Liu et al., 2008, 2012; Santosh et al., 2007a, 2009a, 2012; Shimizu et al., 2013; Yang et al., 2014; Zhang et al., 2012). However, the inferred maximum peak temperature of ~1100°C at Tuguiwula in Liu et al. (2008) and Santosh et al. (2012) might be an overestimation since it was based on a Fe^{3+}-absent FMAS *P*–*T* grid, whereas, Fe^{3+} can reduce the stability of sapphirine to lower temperatures (e.g. Korhonen et al., 2012; Li

and Wei, 2018; Taylor-Jones and Powell, 2010; Wheller and Powell, 2014). Additionally, the inferred T_{max} of 1050°C at Hongsigou (Yang et al., 2014), 1030°C at Heling'er (Liu et al., 2012) and 975°C at Xumayao (Zhang et al., 2012) might also be overestimations as they were only based on spinel–garnet–sillimanite-bearing peak assemblage fields within ZnO-absent pseudosections. Although UHT conditions may have been reached in more rocks than sapphirine-bearing granulites in the Jining region, not all the spinel-bearing garnet–sillimanite gneisses can be directly interpreted to have experienced UHT conditions via the occurrence of spinel unless more evidence (e.g. garnet X_{gr} isopleth) is provided. Caution should be taken when retrieving the peak temperatures of these rocks.

7.1.2. Textural interpretation and P–T path

Spinel is enclosed in the outer margins of garnet (Fig. 3a,b) or in sillimanite (Fig. 3a,b,e,g). We interpret this texture to be a result of modal changes over the metamorphic history, which is illustrated in the simplified sketches in Fig. 11. In the period the pre-peak to peak stages (Fig. 11a → Fig. 11b), there was consumption of garnet and sillimanite and growth of spinel during heating and decompression, producing the inferred peak assemblage containing the paragenesis garnet–sillimanite–spinel. Subsequently, in the post-peak cooling stage (Fig. 11b → Fig. 11c), there was a reduction in the mode of spinel and an increase in the mode of garnet and sillimanite, producing the texture that spinel is included in garnet or sillimanite. In particular, due to the issue of garnet nucleation (e.g. White et al., 2002), spinel close to existing garnet is largely mantled by garnet which is connected to the earlier porphyroblast, in places via a narrow peninsula of garnet. Further growth of garnet tended to occur where garnet was previous consumed (at the garnet boundary),

which resulted in spinel (and/or quartz) enclosed in the outer margins of garnet as observed (Fig. 3a,b). By contrast, spinel distal to garnet porphyroblasts is more commonly enclosed in sillimanite, or rarely feldspar (Fig. 3a,b,e,g).

According to the mineral mode isopleths shown in the pseudosections (Figs 5–7), an overall clockwise *P*–*T* path is required to make the inferred modal changes above possible, although the accurate metamorphic conditions of the prograde evolution cannot be determined. Nevertheless, a post-T_{max} cooling path can be constrained at 8–9 kbar from 980°C to fluid-absent solidus conditions (810–830°C) (Fig. 10). It should be noted that the average temperature of 838°C obtained from the Ti-in-zircon thermometer for sample J1448 is approximately consistent with its fluid-absent solidus condition shown in Fig. 5 (~830°C at 8 kbar), indicating that zircon growth may occur during cooling associated with melt crystallization (e.g. Kelsey and Powell, 2011; Yakymchuk and Brown, 2014; Yakymchuk et al., 2017).

As mentioned above, both clockwise (Li and Wei, 2016, 2018; Yang et al., 2014) and counterclockwise (Liu et al., 2008, 2012; Santosh et al., 2007a, 2009a, 2012; Shimizu et al., 2013; Zhang et al., 2012) *P*–*T* evolutions for the UHT metamorphism in the eastern Khondalite Belt, NCC have been proposed. Regarding the counterclockwise *P*–*T* path, the interpretation is mainly based on the inference that the peak sapphirine–quartz paragenesis in the Tuguiwula UHT rocks was preceded by a spinel–quartz paragenesis (e.g. Santosh et al., 2009a), which may indicate a pre-T_{max} compression path according to the FMAS *P*–*T* grid in Harley (1998). However, the inference that spinel appears prior to sapphirine is arguable and further petrographic observations in Li and Wei (2018) suggest that these two minerals may coexist within the peak assemblage. This means that there might be no robust evidence for the counterclockwise *P*–*T* path. In this study, a clockwise *P*–*T* evolution is more likely. It

is also consistent with the evolution of the extensive 'normal' pelitic granulites in the Jining region, all of which have been interpreted to have clockwise *P–T* paths on the basis of the transition from kyanite to sillimanite (Fig. 12; e.g. Lu and Jin, 1993; Wang et al., 2011). In particular, a clockwise path is consistent with the evolution of UHT granulites at Zhaojiayao (Fig. 12; Li and Wei, 2016), which have been interpreted to have experienced pre-T_{max} decompression based on plagioclase zoning with core–rim increasing X_{An} content.

7.2. Extracting UHT conditions from Fe-rich metapelites through phase equilibrium modelling

As discussed above, Fe-rich UHT metapelites tend to contain neither diagnostic mineral assemblages nor orthopyroxene from which to extract *T* via Al-in-orthopyroxene thermometry. Instead they contain the common garnet–sillimanite-bearing assemblages, which are stable in an extensive field within pseudosections, which makes it difficult for researchers to retrieve UHT conditions. Thus, precise T_{max} conditions for Fe-rich UHT metapelites tend not to be easily obtained through phase equilibrium modelling.

Nevertheless, in this study, UHT conditions have been retrieved from Ca in garnet isopleths within pseudosections (Figs 5–7). By contrast, Mg in garnet isopleths only record temperatures just above the solidus for each sample. This is attributed to Ca diffusion in garnet being much slower than Fe and Mg diffusion (e.g. Chakraborty and Ganguly, 1992), leading to little change in Ca contents during post-T_{max} cooling. However, Ca in garnet in a single sample may not constrain the peak *P–T* conditions well. To refine the *P–T* estimate even further, the measured X_{gr} isopleths of the three samples can be overlapped, and the peak estimate for T_{max} conditions occurs where

the X_{gr} isopleths from the different rocks overlap (Fig. 10). Another example can be found in Hollis et al. (2006), where Ca zoning is preserved in garnet within UHT metapelites.

Additionally, it should be noted that contours of Ca in plagioclase only suggest temperatures above the solidi (Figs 5–7), seemingly inconsistent with the slow diffusion of Ca in plagioclase (e.g. Spear and Florence, 1992). However, this is likely because there is only little plagioclase of relatively small grain size in each sample. As pointed out by Spear and Florence (1992), if only a small proportion of plagioclase exists to re-equilibrate, the greater the extent its composition will change. Another typical example can be found in Li and Wei (2016), where plagioclase in the sample with the highest mode records pre-T_{max} and UHT conditions within pseudosection, but plagioclase in the sample with the lowest mode only records near-solidus conditions.

7.3. Tectonic implications

7.3.1. Timing of the UHT metamorphism

There are two opinions about the timing of the UHT metamorphism in the eastern Khondalite Belt, NCC: (i) *ca*. 1.92 Ga (Santosh et al., 2007b, 2009b, 2013); (ii) *ca*. 1.88 Ga (Yang et al., 2014).

In this study, metamorphic zircons give a mean $^{207}Pb/^{206}Pb$ age of *ca.* 1.91 Ga from garnet–sillimanite gneiss sample J1448 (Fig. 9). This age is inferred to record the post-T_{max} cooling to the solidus (Fig. 10), based on the mean Ti-in-zircon temperature of 838°C, which is lower than the inferred peak temperature and is close to the solidus in pseudosection (Fig. 5). Mantle-derived mafic intrusions with crystallization ages of *ca.* 1.93 Ga, such as the Xuwujia gabbronorites (Peng et al., 2010), are assumed to advect heat for the UHT metamorphism during post-collisional extension (Zhao,

2009). In this case, there may be one prolonged UHT event occuring before *ca*. 1.92 Ga (in this study; Li and Wei, 2016, 2018) and all the ages of *ca.* 1.92, 1.91 and 1.88 Ga record post-peak cooling.

Additionally, the UHT metamorphism must take place later than *ca.* 1.95 Ga as this is the age of the collision-related kyanite-bearing HP pelitic granulites in Qianlishan–Helanshan (Fig. 1b; Yin 2010; Zhou et al., 2010). The reports of 1.97–1.92 Ga mafic magmatic events from Daqingshan (Fig. 1b; Wan et al., 2013) and the *ca.* 1.95 Ga granites which intruded into khondalites in Helanshan (Fig. 1b; Dan et al., 2012) may indicate that extension of the orogen had begun by *ca.* 1.95 Ga. Therefore, in this study, the timing of the peak stage of the UHT metamorphism is interpreted to be *ca.* 1.95–1.92 Ga.

7.3.2. Tectonic regime for the UHT metamorphism

The tectonic regime for the origin of the UHT rocks in the eastern Khondalite Belt, NCC is still controversial. Tectonic models include a plume event (e.g. Santosh et al., 2008), ridge subduction (e.g. Peng et al., 2010; Santosh et al., 2012) and post-collisional mantle upwelling (e.g. Zhao, 2009; Li and Wei, 2018).

In this study, the garnet–sillimanite gneisses at Hongsigou are interpreted to have experienced UHT metamorphism along a clockwise *P–T* path involving pre-T_{max} decompression-heating and post-T_{max} cooling (Fig. 12). The decompression-heating from kyanite-bearing phase assemblage fields, together with the discovery of HP pelitic granulites in Qianlishan–Helanshan (Yin 2010; Zhou et al., 2010) and garnet–sillimanite gneisses containing kyanite inclusions within garnet grains in Jining (Wu et al., 2017), suggests a crustal thickening event at >1.95 Ga (Li and Wei, 2018). This thickening event is deduced to be followed by tectonic extension

beginning at *ca.* 1.95 Ga (e.g. Dan et al., 2012; Wan et al., 2013), during which the UHT metamorphic conditions were reached, in part as a result of heating by mantle-derived magma (Fig. 12). This extension correlates with emplacement of gabbronorites that have intrusion ages of *ca*. 1.93 Ga (Peng et al., 2010) and were likely generated in a post-orogenic setting. Subsequently, cooling of the UHT rocks is interpreted to begin at *ca.* 1.92 Ga, correlating with the occurrence of 1.92–1.90 Ga anatectic S-type granites (Zhong et al., 2007) and both 'normal' and UHT pelitic granulites with ages of 1.92–1.84 Ga (e.g. Cai et al., 2014; Li et al., 2011; Santosh et al., 2007b, 2009b, 2013; Wan et al., 2006; Yang et al., 2014) in the Jining region. According to this tectonic interpretation, the 'normal' and UHT pelitic granulites within the Jining region share a similar geodynamic evolution in which both follow a clockwise *P–T* evolution.

Acknowledgements

This work was financially supported by the National Natural Science Foundation of China (Grant Numbers 41430207 and 41172055) and China Scholarship Council. We thank Fawna Korhonen and P. L. Dharmapriya for their thoughtful reviews of the manuscript, and Marco Scambelluri for his constructive suggestions and editorial work. We also thank Xiaoli Li, Fang Ma and Hong Qin for their help in experimental analyses, and Shiwei Zhang, Xiao Guan and Yue Liao for their involvement in the field work.

References

Brown, M., 2007. Metamorphic conditions in orogenic belts: a record of secular change. Int. Geol. Rev. 49, 193–234.

Cai, J., Liu, F.L., Liu, P.H., Shi, J.R., 2014. Metamorphic *P–T* conditions and U–Pb dating of the

sillimanite–cordierite–garnet paragneisses in Sanchakou, Jining area, Inner Mongolia. Acta Petrol. Sin. 30, 472–490.

Chakraborty, S., Ganguly, J., 1992. Cation diffusion in aluminosilicate garnets: experimental determination in spessartine–almandine diffusion couples, evaluation of effective binary diffusion coefficients, and applications. Contrib. Mineral. Petrol. 111, 74–86.

Condie, K.C., Boryta, M.D., Liu, J.Z., Qian, X.L., 1992. The origin of khondalites: geochemical evidence from the Archean to Early Proterozoic granulite belt in the North China craton. Precambrian Res. 59, 207–223.

Corfu, F., Hanchar, J.M., Hoskin, P.W.O., Kinny, P., 2003. Atlas of zircon textures. Rev. Mineral. Geochem. 53, 469–500.

Dan, W., Li, X.-H., Guo, J.H., Liu, Y., Wang, X.-C., 2012. Integrated in situ zircon U–Pb age and Hf–O isotopes for the Helanshan khondalites in North China Craton: Juvenile crustal materials deposited in active or passive continental margin? Precambrian Res. 222, 143–158.

Diener, J.F.A., White, R.W., Powell, R., 2008. Granulite facies metamorphism and subsolidus fluid- absent reworking, Strangways Range, Arunta Block, central Australia. J. Metamorph. Geol. 26, 603–622.

Dong, C.Y., Liu, D.Y., Li, J.J., Wan, Y.S., Zhou, H.Y., Li, C.D., Yang, Y.H., Xie, L.W., 2007. Palaeoproterozoic Khondalite Belt in the western North China Craton: new evidence from SHRIMP dating and Hf isotope composition of zircons from metamorphic rocks in the Bayan Ul–Helan Mountains area. Chin. Sci. Bull. 52, 2984–2994.

Dong, C.Y., Wan, Y.S., Xu, Z.Y., Liu, D.Y., Yang, Z.S., Ma, M.Z., Xie, H.Q., 2013. SHRIMP zircon U-Pb dating of late Paleoproterozoic kondalites in the Daqing Mountains area on the North China Craton. Sci. China: Earth Sci. 56, 115–125.

Ferry, J.M., Watson, E.B., 2007. New thermodynamic models and revised calibrations for the Ti-in-zircon and Zr-in-rutile thermometers. Contrib. Mineral. Petrol. 154, 429–437.

Fuhrman, M.L., Lindsley, D.H., 1988. Ternary-feldspar modeling and thermometry. Am. Mineral. 73, 201–215.

Guo, J.H., Wang, S.S., Sang, H.Q., Zhai, M.G., 2001. ^{40}Ar–^{39}Ar age spectra of garnet porphyroblast: Implications for metamorphic age of high-pressure granulite in the North

China craton. Acta Petrol. Sin. 17, 436–442.

Harley, S.L., 1998. On the occurrence and characterization of ultrahigh-temperature crustal metamorphism. In: What Drives Metamorphism and Metamorphic Reactions? Special Publication 138. (eds Treloar, P. J. and O'Brien, P. J.), pp. 81–107. Geological Society, London.

Harley, S.L., 2008. Refining the *P–T* records of UHT crustal metamorphism. J. Metamorph. Geol. 26, 125–154.

Harley, S.L., Motoyoshi, Y., 2000. Al zoning in orthopyroxene in a sapphirine quartzite: evidence for >1120 °C UHT metamorphism in the Napier Complex, Antarctica, and implications for the entropy of sapphirine. Contrib. Mineral. Petrol. 138, 293–307.

Hensen, B.J., Green, D.H., 1973. Experimental study of the stability of cordierite and garnet in pelitic compositions at high pressures and temperatures. Contrib. Mineral. Petrol. 38, 151–166.

Holland, T., Powell, R., 2003. Activity–composition relations for phases in petrological calculations: an asymmetric multicomponent formulation. Contrib. Mineral. Petrol. 145, 492–501.

Holland, T.J.B., Powell, R., 2011. An improved and extended internally consistent thermodynamic dataset for phases of petrological interest, involving a new equation of state for solids. J. Metamorph. Geol. 29, 333–383.

Hollis, J.A., Harley, S.L., White, R.W., Clarke, G.L., 2006. Preservation of evidence for prograde metamorphism in ultrahigh-temperature, high-pressure kyanite-bearing granulites, South Harris, Scotland. J. Metamorph. Geol. 24, 263–279.

Jiao, S.J., Guo, J.H., 2011. Application of the two-feldspar geothermometer to ultrahigh-temperature (UHT) rocks in the Khondalite belt, North China craton and its implications. Am. Mineral. 96, 250–260.

Jiao, S.J., Guo, J.H., Harley, S.L., Peng, P., 2013. Geochronology and trace element geochemistry of zircon, monazite and garnet from the garnetite and/or associated other high-grade rocks: Implications for Palaeoproterozoic tectonothermal evolution of the Khondalite Belt, North China Craton. Precambrian Res. 237, 78–100.

Kelsey, D.E., 2008. On ultrahigh-temperature crustal metamorphism. Gondwana Res. 13, 1–29.

Kelsey, D.E., Powell, R., 2011. Progress in linking accessory mineral growth and breakdown to major mineral evolution in metamorphic rocks: a thermodynamic approach in the Na_2O–CaO–K_2O–FeO–MgO–Al_2O_3–SiO_2–H_2O–TiO_2–ZrO_2 system. J. Metamorph. Geol. 29, 151–166.

Kelsey, D.E., White, R.W., Powell, R., 2003. Orthopyroxene–sillimanite–quartz assemblages: distribution, petrology, quantitative *P–T–X* constraints and *P–T* paths. J. Metamorph. Geol. 21, 439–453.

Korhonen, F.J., Saw, A.K., Clark, C., Brown, M., Bhattacharya, S., 2011. New constraints on UHT metamorphism in the Eastern Ghats Province through the application of phase equilibria modelling and in situ geochronology. Gondwana Res. 20, 764–781.

Korhonen, F.J., Powell, R., Stout, J.H., 2012. Stability of sapphirine plus quartz in the oxidized rocks of the Wilson Lake terrane, Labrador: calculated equilibria in NCKFMASHTO. J. Metamorph. Geol. 30, 21–36.

Li, X.W., Wei, C.J., 2016. Phase equilibria modelling and zircon age dating of pelitic granulites in Zhaojiayao, from the Jining Group of the Khondalite Belt, North China Craton. J. Metamorph. Geol. 34, 595–615.

Li, X.W., Wei, C.J., 2018. Ultrahigh- temperature metamorphism in the Tuguiwula area, Khondalite Belt, North China Craton. J. Metamorph. Geol. 36, 489–509.

Li, X.-P., Yang, Z.Y., Zhao, G.C., Grapes, R., Guo, J.H., 2011. Geochronology of khondalite-series rocks of the Jining Complex: confirmation of depositional age and tectonometamorphic evolution of the North China craton. Int. Geol. Rev. 53, 1194–1211.

Liu, S.J., Li, J.H., Santosh, M., 2008. Ultrahigh temperature metamorphism of Tuguiwula khondalite belt, Inner Mongolia: Metamorphic reaction texture and *P–T* indication. Acta Petrol. Sin. 24, 1185–1192.

Liu, S.J., Tsunogae, T., Li, W.S., Shimizu, H., Santosh, M., Wan, Y.S., Li, J.H., 2012. Paleoproterozoic granulites from Heling'er: Implications for regional ultrahigh-temperature metamorphism in the North China Craton. Lithos 148, 54–70.

Lu, L.Z., Jin, S.Q., 1993. *P–T–t* paths and tectonic history of an early Precambrian granulite facies

terrane, Jining district, south-east Inner Mongolia, China. J. Metamorph. Geol. 11, 483–498.

Lu, L.Z., Jin, S.Q., Xu, X.T., Liu, F.L., 1992. Petrogenesis and Mineralization of Khondalite Series in Southeastern Inner Mongolia. Jilin Science and Technology Press, Changchun.

Lu, L.Z., Xu, X.C., Liu, F.L., 1996. Early Precambrian Khondalite Series in North China. Changchun Publishing House, Changchun.

Ludwig, K.R., 2003. User's Manual for Isoplot 3.00: A Geochronological Toolkit for Microsoft Excel (No. 4). Kenneth R. Ludwig, Berkeley Geochronology Center, Berkeley, CA.

Nichols, G.T., Berry, R.F., Green, D.H., 1992. Internally consistent gahnitic spinel–cordierite–garnet equilibria in the FMASHZn system: geothermobarometry and applications. Contrib. Mineral. Petrol. 111, 362–377.

Peng, P., Guo, J.H., Zhai, M.G., Bleeker, W., 2010. Paleoproterozoic gabbronoritic and granitic magmatism in the northern margin of the North China Craton: evidence of crust–mantle interaction. Precambrian Res. 183, 635–659.

Powell, R., Holland, T.J.B., 1988. An internally consistent dataset with uncertainties and correlations: 3. Applications to geobarometry, worked examples and a computer program. J. Metamorph. Geol. 6, 173–204.

Powell, R., White, R.W., Green, E.C.R., Holland, T.J.B., Diener, J.F.A., 2014. On parameterizing thermodynamic descriptions of minerals for petrological calculations. J. Metamorph. Geol. 32, 245–260.

Qian, J.H., Wei, C.J., 2016. *P–T–t* evolution of garnet amphibolites in the Wutai–Hengshan area, North China Craton: insights from phase equilibria and geochronology. J. Metamorph. Geol. 34, 423–446.

Qian, J.H., Wei, C.J., Zhou, X.W., Zhang, Y.H., 2013. Metamorphic *P–T* paths and New Zircon U–Pb age data for garnet–mica schist from the Wutai Group, North China Craton. Precambrian Res. 233, 282–296.

Qian, J.H., Wei, C.J., Clarke, G.L., Zhou, X.W., 2015. Metamorphic evolution and Zircon ages of Garnet–orthoamphibole rocks in southern Hengshan, North China Craton: Insights into the regional Paleoproterozoic *P–T–t* history. Precambrian Res. 256, 223–240.

Rosenberg, C.L., Handy, M.R., 2005. Experimental deformation of partially melted granite

revisited: implications for the continental crust. J. Metamorph. Geol. 23, 19–28.

Santosh, M., Tsunogae, T., Li, J.H., Liu, S.J., 2007a. Discovery of sapphirine-bearing Mg–Al granulites in the North China Craton: implications for Paleoproterozoic ultrahigh temperature metamorphism. Gondwana Res. 11, 263–285.

Santosh, M., Wilde, S.A., Li, J.H., 2007b. Timing of Paleoproterozoic ultrahigh-temperature metamorphism in the North China Craton: evidence from SHRIMP U–Pb zircon geochronology. Precambrian Res. 159, 178–196.

Santosh, M., Tsunogae, T., Ohyama, H., Sato, K., Li, J.H., Liu, S.J., 2008. Carbonic metamorphism at ultrahigh-temperatures: evidence from North China Craton. Earth Planet. Sci. Lett. 266, 149–165.

Santosh, M., Sajeev, K., Li, J.H., Liu, S.J., Itaya, T., 2009a. Counterclockwise exhumation of a hot orogen: the Paleoproterozoic ultrahigh-temperature granulites in the North China Craton. Lithos 110, 140–152.

Santosh, M., Wan, Y.S., Liu, D.Y., Dong, C.Y., Li, J.H., 2009b. Anatomy of Zircons from an Ultrahot Orogen: The Amalgamation of the North China Craton within the Supercontinent Columbia. J. Geol. 117, 429–443.

Santosh, M., Liu, S.J., Tsunogae, T., Li, J.H., 2012. Paleoproterozoic ultrahigh-temperature granulites in the North China Craton: implications for tectonic models on extreme crustal metamorphism. Precambrian Res. 222, 77–106.

Santosh, M., Liu, D.Y., Shi, Y.R., Liu, S.J., 2013. Paleoproterozoic accretionary orogenesis in the North China Craton: a SHRIMP zircon study. Precambrian Res. 227, 29–54.

Shimizu, H., Tsunogae, T., Santosh, M., Liu, S.J., Li, J.H., 2013. Phase equilibrium modelling of Palaeoproterozoic ultrahigh- temperature sapphirine granulite from the Inner Mongolia Suture Zone, North China Craton: implications for counterclockwise *P–T* path. Geol. J. 48, 456–466.

Spear, F.S., Florence, F.P., 1992. Thermobarometry in granulites: pitfalls and new approaches. Precambrian Res. 55, 209–241.

Taylor- Jones, K., Powell, R., 2010. The stability of sapphirine + quartz: calculated phase equilibria in FeO–MgO–Al_2O_3–SiO_2–TiO_2–O. J. Metamorph. Geol. 28, 615–633.

Tomkins, H.S., Powell, R., Ellis, D.J., 2007. The pressure dependence of the zirconium- in- rutile thermometer. J. Metamorph. Geol. 25, 703–713.

Van Achterbergh, E., Ryan, C.G., Jackson, S.E., Griffin, W.L., 2001. Data reduction software for LA-ICP-MS. Data reduction software for LA-ICP-MS. In: LaserAblation-ICPMS in the Earth Sciences: Principles and Applications, vol. 29 (ed Sylvester, P.), pp. 239–243. Mineralogical Society of Canada, Ottawa, Canada.

Vavra, G., Gebauer, D., Schmid, R., Compston, W., 1996. Multiple zircon growth and recrystallization during polyphase Late Carboniferous to Triassic metamorphism in granulites of the Ivrea Zone (Southern Alps): an ion microprobe (SHRIMP) study. Contrib. Mineral. Petrol. 122, 337–358.

Wan, Y.S., Song, B., Liu, D.Y., Wilde, S.A., Wu, J.S., Shi, Y.R., Yin, X.Y., Zhou, H.Y., 2006. SHRIMP U–Pb zircon geochronology of Palaeoproterozoic metasedimentary rocks in the North China Craton: evidence for a major Late Palaeoproterozoic tectonothermal event. Precambrian Res. 149, 249–271.

Wan, Y.S., Xu, Z.Y., Dong, C.Y., Nutman, A., Ma, M.Z., Xie, H.Q., Liu, S.J., Liu, D.Y., Wang, H.C., Cu, H., 2013. Episodic Paleoproterozoic (~2.45, ~1.95 and ~1.85 Ga) mafic magmatism and associated high temperature metamorphism in the Daqingshan area, North China Craton: SHRIMP zircon U–Pb dating and whole-rock geochemistry. Precambrian Res. 224, 71–93.

Wang, F., Li, X.P., Chu, H., Zhao, G.C., 2011. Petrology and metamorphism of khondalites from the Jining complex, North China craton. Int. Geol. Rev. 53, 212–229.

Wei, C.J., Qian, J.H., Zhou, X.W., 2014. Paleoproterozoic crustal evolution of the Hengshan–Wutai–Fuping region, North China Craton. Geosci. Front. 5, 485–497.

Wheller, C.J., Powell, R., 2014. A new thermodynamic model for sapphirine: calculated phase equilibria in K_2O–FeO–MgO–Al_2O_3–SiO_2–H_2O–TiO_2–Fe_2O_3. J. Metamorph. Geol. 32, 287–299.

White, R.W., Powell, R., Holland, T.J.B., Worley, B.A., 2000. The effect of TiO_2 and Fe_2O_3 on metapelitic assemblages at greenschist and amphibolite facies conditions: mineral equilibria calculations in the system K_2O–FeO–MgO–Al_2O_3–SiO_2–H_2O–TiO_2–Fe_2O_3. J. Metamorph.

Geol. 18, 497–512.

White, R.W., Powell, R., Clarke, G.L., 2002. The interpretation of reaction textures in Fe- rich metapelitic granulites of the Musgrave Block, central Australia: constraints from mineral equilibria calculations in the system K_2O–FeO–MgO–Al_2O_3–SiO_2–H_2O–TiO_2–Fe_2O_3. J. Metamorph. Geol. 20, 41–55.

White, R.W., Powell, R., Halpin, J.A., 2004. Spatially-focussed melt formation in aluminous metapelites from Broken Hill, Australia. J. Metamorph. Geol. 22, 825–845.

White, R.W., Powell, R., Holland, T.J.B., 2007. Progress relating to calculation of partial melting equilibria for metapelites. J. Metamorph. Geol. 25, 511–527.

White, R.W., Powell, R., Holland, T.J.B., Johnson, T.E., Green, E.C.R., 2014a. New mineral activity–composition relations for thermodynamic calculations in metapelitic systems. J. Metamorph. Geol. 32, 261–286.

White, R.W., Powell, R., Johnson, T.E., 2014b. The effect of Mn on mineral stability in metapelites revisited: new *a–x* relations for manganese- bearing minerals. J. Metamorph. Geol. 32, 809–828.

Wiedenbeck, M., Alle, P., Corfu, F., Griffin, W.L., Meier, M., Oberli, F., Vonquadt, A., Roddick, J.C., Speigel, W., 1995. Three natural zircon standards for U–Th–Pb, Lu–Hf, trace element and REE analyses. Geostand. Newsl. 19, 1–23.

Wiedenbeck, M., Hanchar, J.M., Peck, W.H., Sylvester, P., Valley, J., Whitehouse, M., Kronz, A., Morishita, Y., Nasdala, L., Fiebig, J., Franchi, I., Girard, J.P., Greenwood, R.C., Hinton, R., Kita, N., Mason, P.R.D., Norman, M., Ogasawara, M., Piccoli, R., Rhede, D., Satoh, H., Schulz-Dobrick, B., Skar, O., Spicuzza, M.J., Terada, K., Tindle, A., Togashi, S., Vennemann, T., Xie, Q., Zheng, Y.F., 2004. Further characterisation of the 91500 zircon crystal. Geostand. Geoanal. Res. 28, 9–39.

Wu, J.L., Zhang, H.F., Zhai, M.G., Guo, J.H., Li, R.X., Wang, H.Z., Zhao, L., Jia, X.L., Wang, L.J., Hu, B., Zhang, H.D., 2017. Paleoproterozoic high-pressure-high-temperature pelitic granulites from Datong in the North China Craton and their geological implications: Constraints from petrology and phase equilibrium modeling. Precambrian Res. 303, 727–748.

Yakymchuk, C., Brown, M., 2014. Behaviour of zircon and monazite during crustal melting. J. Geol. Soc. (London, U. K.) 171, 465–479.

Yakymchuk, C., Clark, C., White, R.W., 2017. Phase relations, reaction sequences and petrochronology. Rev. Mineral. Geochem. 83, 13–53.

Yang, Q.-Y., Santosh, M., Tsunogae, T., 2014. Ultrahigh-temperature metamorphism under isobaric heating: New evidence from the North China Craton. J. Asian Earth Sci. 95, 2–16.

Yin, C.Q., 2010. Metamorphism of the Helanshan–Qianlishan Complex and its implications for tectonic evolution of the khondalite belt in the western block, North China Craton. HKU Theses Online (HKUTO), Hong Kong.

Zhai, M.G., Peng, P., 2007. Paleoproterozoic events in the North China craton. Acta Petrol. Sin. 23, 2665–2682.

Zhang, H.T., Li, J.H., Liu, S.J., Li, W.S., Santosh, M., Wang, H.H., 2012. Spinel + quartz-bearing ultrahigh-temperature granulites from Xumayao, Inner Mongolia Suture Zone, North China Craton: Petrology, phase equilibria and counterclockwise *p–T* path. Geosci. Front. 3, 603–611.

Zhang, Y.H., Wei, C.J., Tian, W., Zhou, X.W., 2013. Reinterpretation of metamorphic age of the Hengshan Complex, North China Craton. Chin. Sci. Bull. 58, 4300–4307.

Zhao, G.C., 2009. Metamorphic evolution of major tectonic units in the basement of the North China Craton: key issues and discussion. Acta Petrol. Sin. 25, 1772–1792.

Zhao, G.C., Wilde, S.A., Cawood, P.A., Lu, L.Z., 1998. Thermal evolution of Archean basement rocks from the eastern part of the North China Craton and its bearing on tectonic setting. Int. Geol. Rev. 40, 706–721.

Zhao, G.C., Sun, M., Wilde, S.A., Li, S.Z., 2005. Late Archean to Paleoproterozoic evolution of the North China Craton: key issues revisited. Precambrian Res. 136, 177–202.

Zhao, G.C., Cawood, P.A., Li, S.Z., Wilde, S.A., Sun, M., Zhang, J., He, Y.H., Yin, C.Q., 2012. Amalgamation of the North China Craton: key issues and discussion. Precambrian Res. 222, 55–76.

Zhong, C.T., Deng, J.F., Wan, Y.S., Mao, D.B., Li, H.M., 2007. Magma recording of Paleoproterozoic orogeny in central segment of northern margin of North China Craton:

Geochemical characteristics and zircon SHRIMP dating of S-type granitoids. Geochimica 36, 633–637.

Zhou, X.W., Zhao, G.C., Geng, Y.S., 2010. Helanshan high pressure pelitic granulite: Petrologic evidence for collision event in the western block of the North China Craton. Acta Petrol. Sin. 26, 2113–2121.

Figure and table captions

Fig. 1. (a) Tectonic division of the North China Craton (modified after Zhao et al. (2005) and Cai et al. (2014)). (b) Tectonic subdivision of the Western Block into the Ordos and Yinshan Blocks, which are separated by the E–W-striking Paleoproterozoic Khondalite Belt (modified after Zhao et al. (2005)). (c) Geological map of the Jining region (modified after Guo et al. (2001)) showing UHT metapelite localities: (1) Tuguiwula (Li and Wei, 2018; Santosh et al., 2007a; Shimizu et al., 2013); (2) Xuwujia (Jiao and Guo, 2011; Li and Wei, 2018; Santosh et al., 2009a); (3) Hongsigou (Yang et al., 2014); (4) Zhaojiayao (Li and Wei, 2016); (5) Heling'er (Liu et al., 2012) and (6) Xumayao (Zhang et al., 2012)

Fig. 2. Field photographs of garnet–sillimanite gneisses (a,b,c) and garnet-bearing S-type granites (d). (a) Gneisses that contain less melanocratic minerals (e.g. biotite, sillimanite) are light-coloured. (b) Gneisses that contain more melanocratic minerals are dark-coloured. (c) Garnet-bearing leucosomes occur within the gneisses

Fig. 3. Photomicrographs of garnet–sillimanite gneisses. Boundaries of garnet grains are contoured by dashed line in (a), (b) and (d). (a) Spinel is included in sillimanite and in the outer margins of garnet (sample J1448). (b) Spinel is included in sillimanite, in the outer margins of garnet and in plagioclase within K-feldspar (sample J1448). (c)

Matrix mainly consists of sillimanite, K-feldspar, plagioclase, quartz and biotite (sample J1448). (d) Garnet porphyroblast has inclusions of biotite, quartz and fibrolitic sillimanite (sample J1542). (e) Sillimanite occurs as columnar crystals in the matrix with inclusions of spinel (sample J1542). (f) Matrix mainly consists of sillimanite, K-feldspar, plagioclase, quartz and biotite (sample J1542). (g) Spinel is included in columnar sillimanite in the matrix (sample J1544). (h) Matrix mainly consists of sillimanite, K-feldspar, plagioclase, quartz and biotite (sample J1544). The mineral abbreviations are as follows: bi – biotite; g – garnet; ilm – ilmenite; ksp – K-feldspar; pl – plagioclase; q – quartz; ru – rutile; sill – sillimanite; sp – spinel

Fig. 4. Ti (pfu) – Mg/(Mg+Fe^{2+}) diagram showing biotite compositions in this study

Fig. 5. (a) *P–T* pseudosection with proposed *P–T* path for sample J1448. (b) Blowup showing changes in mineral modes. The mineral abbreviations are as follows: cd – cordierite; ky – kyanite; liq – silicate liquid/melt; opx – orthopyroxene; other abbreviations are the same as those in Fig. 3. The composition used for modelling is listed in Table 4

Fig. 6. (a) *P–T* pseudosection with proposed *P–T* path for sample J1542. (b) Blowup showing changes in mineral modes. Other details are the same as those in Fig. 5

Fig. 7. (a) *P–T* pseudosection with proposed *P–T* path for sample J1544. (b) Blowup showing changes in mineral modes. Other details are the same as those in Fig. 5

Fig. 8. Cathodoluminescence (CL) images of selected zircons in sample J1448.

Circles illustrate positions of LA-ICP-MS analytical sites with their identification numbers as in Table 5

Fig. 9. Concordia diagrams showing LA-ICP-MS U–Pb data of sample J1448

Fig. 10. *P–T* evolution of the garnet–sillimanite gneisses at Hongshaba. The solidus assemblage fields for samples J1448, J1542 and J1544 are labelled with (1), (2) and (3) respectively

Fig. 11. Inferred textural development and modal changes of the Hongshaba metapelites. As the textures mostly involve garnet, spinel, sillimanite and quartz, only these minerals are shown in the simplified sketches

Fig. 12. *P–T* paths for the 'normal' pelitic granulites are labelled with (1) (Wang et al., 2011) and (2) (Cai et al., 2014) from the Jining region and the *P–T* path for the HP pelitic granulites is labeled with (3) (Yin, 2010) from the Qianlishan–Helanshan area. The *P–T* paths for the UHT pelitic granulites are labelled with (4) (Li and Wei, 2016), (5) (Li and Wei, 2018), (6) (Santosh et al., 2012), (7) (Shimizu et al., 2013), (8) (Liu et al., 2008) and (9) (Yang et al., 2014) from the Jining region. The *P–T* path in this study is labeled with (10). The abbreviations are as follows: NG – 'normal' granulites; UHTG – ultrahigh-temperature granulites; E-HPG – eclogite–high-pressure granulites. The effective sub-aluminous pelite solidus and areas of NG, UHTG and E-HPG are cited from Brown (2007). The transition lines of Al_2SiO_5 were calculated using THERMOCALC

Table 1 Representative mineral analyses for samples J1448 and J1542

Table 2 Representative mineral analyses for sample J1544

Table 3 Bulk-rock compositions of garnet–sillimanite gneiss samples in this study (wt%)

Table 4 Molar proportions used for phase equilibrium modelling (mol.%)

Table 5 Zircon U–Pb isotope data, Ti-concentration in zircons and calculated temperatures using the Ti-in-zircon thermometer

Table 1 Representative mineral analyses for samples J1448 and J1542

	J1448							J1542					
Mine	g	bi-	bi	ksp	pl	pl-	sp	g	bi-	bi	ksp	pl	sp
SiO_2	39.7	38.	38.	64.	57.9	57.	0.0	38.	37.	38.	64.	61.	0.0
TiO_2	0.02	3.9	5.0	0.0	0.05	0.0	0.0	0.0	6.7	3.7	0.0	0.0	0.0
Al_2O_3	22.2	15.	15.	18.	27.4	26.	61.	21.	15.	15.	18.	24.	59.
Cr_2O_3	0.05	0.0	0.0	0.0	0.07	0.0	0.3	0.0	0.0	0.0	0.0	0.0	0.5
FeO^T	25.5	6.8	11.	0.1	0.05	0.1	23.	27.	8.6	10.	0.0	0.0	24.
MnO	0.43	0.0	0.0	0.0	0.04	0.0	0.0	0.3	0.0	0.0	0.0	0.0	0.0
MgO	11.3	19.	15.	0.0	0.01	0.0	11.	10.	16.	16.	0.0	0.0	8.9
CaO	1.35	0.0	0.0	0.2	8.05	8.9	0.0	0.9	0.0	0.0	0.2	5.8	0.0
Na_2O	0.04	0.2	0.1	1.5	7.10	6.4	0.0	0.0	0.2	0.1	1.7	8.1	0.0
K_2O	0.03	9.4	9.3	14.	0.17	0.0	0.0	0.0	9.1	9.2	13.	0.1	0.0
NiO							0.3						0.1
ZnO							2.6						5.1
Total	100.	94.	95.	99.	100.	99.	99.	99.	93.	94.	99.	99.	99.
O	12	11	11	8	8	8	4	12	11	11	8	8	4
Si	2.99	2.8	2.7	2.9	2.57	2.5	0.0	2.9	2.7	2.8	2.9	2.7	0.0
Ti	0.00	0.2	0.2	0.0	0.00	0.0	0.0	0.0	0.3	0.2	0.0	0.0	0.0
Al	1.98	1.3	1.3	1.0	1.43	1.4	1.9	1.9	1.3	1.3	1.0	1.2	1.9
Cr	0.00	0.0	0.0	0.0	0.00	0.0	0.0	0.0	0.0	0.0	0.0	0.0	0.0
Fe^{3+}	0.04	0.0	0.0	0.0	0.00	0.0	0.0	0.0	0.0	0.0	0.0	0.0	0.0
Fe^{2+}	1.56	0.4	0.7	0.0	0.00	0.0	0.4	1.6	0.5	0.6	0.0	0.0	0.5
Mn	0.03	0.0	0.0	0.0	0.00	0.0	0.0	0.0	0.0	0.0	0.0	0.0	0.0
Mg	1.28	2.0	1.7	0.0	0.00	0.0	0.4	1.1	1.8	1.8	0.0	0.0	0.3
Ca	0.11	0.0	0.0	0.0	0.38	0.4	0.0	0.0	0.0	0.0	0.0	0.2	0.0
Na	0.01	0.0	0.0	0.1	0.61	0.5	0.0	0.0	0.0	0.0	0.1	0.7	0.0
K	0.00	0.8	0.8	0.8	0.01	0.0	0.0	0.0	0.8	0.8	0.8	0.0	0.0
Ni							0.0						0.0
Zn							0.0						0.1
X(pha	0.43	0.8	0.7	0.8	0.38	0.4	0.4	0.4	0.7	0.7	0.8	0.2	0.4
Y(pha	0.04							0.0					

X(g) = Mg/(Fe^{2+} + Mg + Ca); *X*(bi, sp) = Mg/(Mg + Fe^{2+}); *X*(pl) = Ca/(Ca + Na + K); *X*(ksp) = K/(Ca + Na + K); *Y*(g) = Ca/(Fe^{2+} + Mg + Ca); -G, within garnet grains; -SP, around spinel. The mineral abbreviations are the same as those in Fig. 3

Table 2 Representative mineral analyses for sample J1544

	J1544					
Mineral	g	bi-G	bi	ksp	pl	sp
SiO_2	38.64	38.46	37.17	64.96	61.24	0.05
TiO_2	0.00	4.15	4.97	0.11	0.00	0.03
Al_2O_3	21.70	14.74	14.95	18.61	23.98	56.44
Cr_2O_3	0.00	0.12	0.03	0.02	0.01	0.98
FeO^T	27.93	8.73	11.95	0.00	0.02	30.12
MnO	0.50	0.01	0.00	0.04	0.02	0.07
MgO	10.03	18.45	15.62	0.00	0.00	7.75
CaO	0.89	0.00	0.00	0.13	5.57	0.00
Na_2O	0.00	0.19	0.15	1.75	8.26	0.00
K_2O	0.00	9.25	9.47	13.58	0.21	0.01
NiO						0.17
ZnO						3.86
Total	99.69	94.10	94.31	99.20	99.31	99.49
O	12	11	11	8	8	4
Si	2.98	2.82	2.77	2.99	2.74	0.00
Ti	0.00	0.23	0.28	0.00	0.00	0.00
Al	1.97	1.27	1.31	1.01	1.26	1.86
Cr	0.00	0.01	0.00	0.00	0.00	0.02
Fe^{3+}	0.08	0.00	0.00	0.00	0.00	0.11
Fe^{2+}	1.72	0.53	0.74	0.00	0.00	0.60
Mn	0.03	0.00	0.00	0.00	0.00	0.00
Mg	1.15	2.01	1.73	0.00	0.00	0.32
Ca	0.07	0.00	0.00	0.01	0.27	0.00
Na	0.00	0.03	0.02	0.16	0.72	0.00
K	0.00	0.86	0.90	0.80	0.01	0.00
Ni						0.00
Zn						0.08
X(phase)	0.39	0.79	0.70	0.83	0.27	0.35
Y(phase)	0.02					

Details are the same as those in Table 1

Table 3 Bulk-rock compositions of garnet–sillimanite gneiss samples in this study (wt%)

Sample	SiO_2	TiO_2	Al_2O_3	$Fe_2O_3^T$	MnO	MgO	CaO	Na_2O	K_2O	P_2O_5	LOI	Total	Fe^{3+}/Fe^T	$Mg/(Mg+Fe^T)$
J1448	65.05	0.78	16.11	8.98	0.11	3.61	0.99	0.76	2.88	0.05	0.38	99.70	0.04	0.44
J1542	64.06	0.71	19.39	6.83	0.06	2.95	0.60	1.11	3.42	0.01	1.12	100.27	0.03	0.46
J1544	61.81	0.88	18.20	8.74	0.09	3.40	0.95	1.52	3.36	0.11	0.18	99.23	0.01	0.44

Fe^{3+}/Fe^T values are determined by Fe^{2+} titration

Table 4 Molar proportions used for phase equilibrium modelling (mol.%)

Sample	H_2O	SiO_2	Al_2O_3	CaO	MgO	FeO	K_2O	Na_2O	TiO_2	O
J1448	0.93	70.85	10.34	1.08	5.86	7.36	2.00	0.80	0.64	0.14
J1542	1.29	70.64	12.60	0.69	4.85	5.67	2.41	1.19	0.59	0.08
J1544	1.01	68.47	11.88	0.96	5.61	7.29	2.37	1.63	0.73	0.05

Table 5 Zircon U–Pb isotope data, Ti-concentration in zircons and calculated temperatures using the Ti-in-zircon thermometer

Spot	Th (ppm)	U (ppm)	Th/U	Measured isotope ratios						Corrected ages (Ma)						D (%)	Ti (ppm)	T (°C)
				$^{207}Pb/^{20}$	1σ	$^{207}Pb/$	1σ	$^{206}Pb/$	1σ	$^{207}Pb/^{20}$	1σ	$^{207}Pb/$	1σ	$^{206}Pb/$	1σ			
J14	5	4	1.	0.11	0.	5.4	0.	0.3	0.	189	2	189	1	189	2	0.	3	8
J14	6	5	1.	0.11	0.	5.5	0.	0.3	0.	190	1	190	1	191	2	-	3	8
J14	9	8	1.	0.11	0.	5.6	0.	0.3	0.	192	1	191	1	191	2	0.	2	8
J14	1	5	2.	0.11	0.	5.4	0.	0.3	0.	187	1	190	1	192	2	-	2	8
J14	2	2	1.	0.11	0.	5.6	0.	0.3	0.	193	1	193	1	192	1	0.	3	8
J14	2	2	1.	0.11	0.	5.5	0.	0.3	0.	190	1	190	1	190	1	0.	2	8
J14	2	1	1.	0.11	0.	5.5	0.	0.3	0.	190	1	190	1	190	1	0.	2	8
J14	9	7	1.	0.11	0.	5.7	0.	0.3	0.	194	2	194	1	194	2	0.	2	8
J14	9	5	1.	0.11	0.	5.5	0.	0.3	0.	191	1	191	1	190	2	0.	2	8
J14	2	1	1.	0.11	0.	5.5	0.	0.3	0.	188	1	190	1	191	1	-	3	8
J14	4	1	0.	0.11	0.	5.6	0.	0.3	0.	192	1	191	1	191	1	0.	2	8
J14	6	5	1.	0.11	0.	5.4	0.	0.3	0.	190	1	189	1	189	2	0.	2	8
J14	7	8	0.	0.11	0.	5.2	0.	0.3	0.	187	1	186	1	186	1	0.	11	7
J14	2	1	1.	0.11	0.	5.4	0.	0.3	0.	189	1	189	1	189	1	0.	1	7
J14	1	6	2.	0.11	0.	5.6	0.	0.3	0.	192	1	191	1	191	2	0.	2	8
J14	1	6	1.	0.11	0.	5.5	0.	0.3	0.	191	1	190	1	190	2	0.	2	8
J14	9	7	1.	0.11	0.	5.6	0.	0.3	0.	193	1	192	1	192	2	0.	1	8
J14	9	6	1.	0.11	0.	5.6	0.	0.3	0.	192	1	191	1	191	2	0.	2	8
J14	7	2	0.	0.11	0.	5.5	0.	0.3	0.	190	1	190	1	191	1	-	1	8
J14	8	5	1.	0.11	0.	5.5	0.	0.3	0.	190	1	190	1	190	2	0.	2	8
J14	2	2	1.	0.11	0.	5.4	0.	0.3	0.	190	1	189	1	189	1	0.	2	8
J14	6	4	1.	0.11	0.	5.5	0.	0.3	0.	191	2	190	1	190	2	0.	3	8
J14	3	2	0.	0.11	0.	5.6	0.	0.3	0.	192	1	192	1	191	1	0.	2	8
J14	6	5	1.	0.11	0.	5.4	0.	0.3	0.	189	2	188	1	188	2	0.	2	8
J14	3	2	1.	0.11	0.	5.7	0.	0.3	0.	194	1	193	1	193	1	0.	3	8
J14	9	6	1.	0.11	0.	5.6	0.	0.3	0.	192	1	192	1	191	2	0.	2	8
J14	1	11	0.	0.11	0.	5.5	0.	0.3	0.	190	1	190	1	190	1	0.	1	8
J14	8	5	1.	0.11	0.	5.6	0.	0.3	0.	193	2	192	1	192	2	0.	3	8
J14	8	5	1.	0.11	0.	5.5	0.	0.3	0.	189	2	190	1	190	2	-	2	8
J14	7	1	0.	0.11	0.	5.5	0.	0.3	0.	193	1	190	1	188	1	2.	1	8
J14	2	1	1.	0.11	0.	5.5	0.	0.3	0.	190	1	190	1	190	1	0.	3	8
J14	2	1	1.	0.11	0.	5.4	0.	0.3	0.	190	1	189	1	189	1	0.	3	8
J14	2	2	1.	0.11	0.	5.3	0.	0.3	0.	187	1	187	1	186	1	0.	2	8
J14	9	8	1.	0.11	0.	5.4	0.	0.3	0.	190	1	189	1	188	2	0.	2	8
J14	2	2	0.	0.11	0.	5.6	0.	0.3	0.	192	1	191	1	191	1	0.	2	8

1σ refers to 1 sigma of standard deviation. Degree of discordance = 100 × (1 – $^{206}Pb/^{238}U$ age/$^{207}Pb/^{206}Pb$ age)

Highlights

- Metapelites at Hongshaba, North China Craton have experienced UHT metamorphism
- Ca in garnet may aid in retrieving UHT conditions from Fe-rich metapelites
- An overall clockwise *P–T* evolution is likely for Hongshaba UHT rocks
- The timing of cooling of Hongshaba UHT rocks to solidus is *ca*. 1.91 Ga

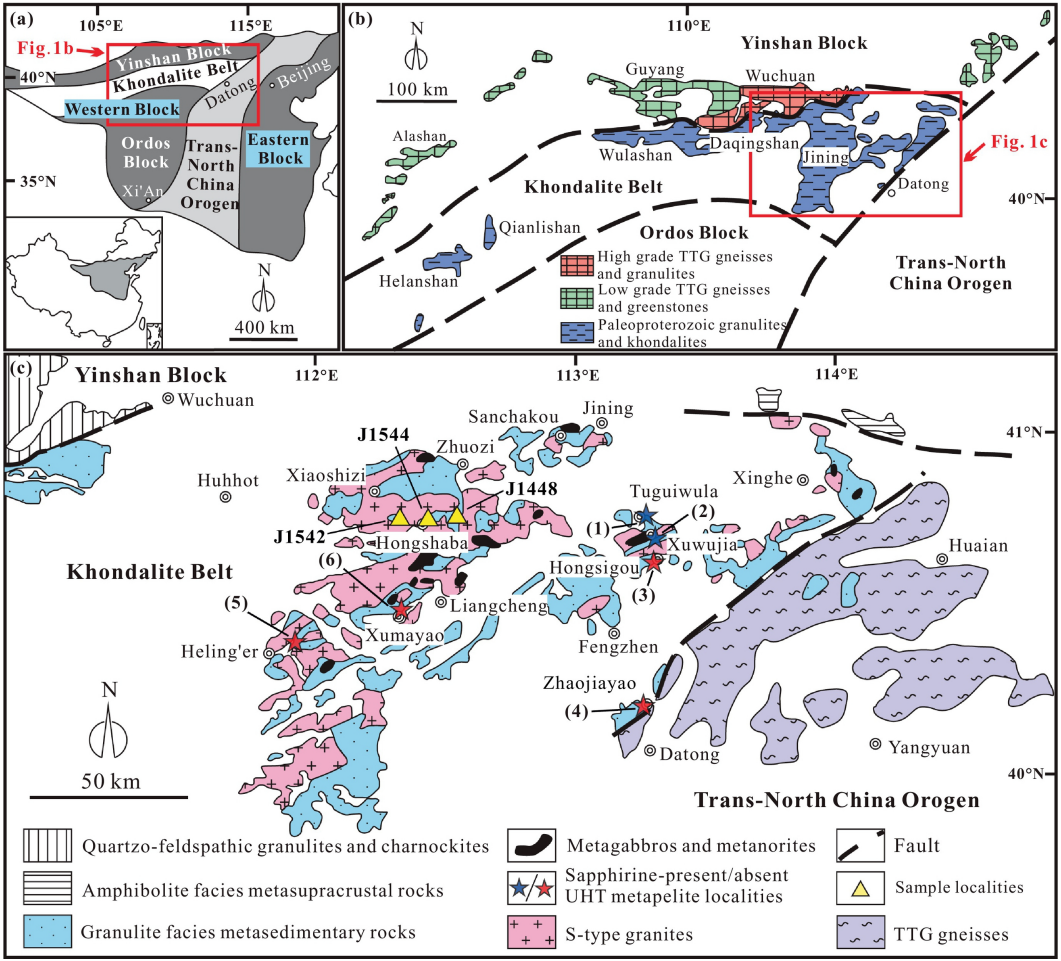
(a)
105°E
115°E
Fig.1b
Yinshan Block
Khondalite Belt
Datong
Beijing
40°N
Western Block
Ordos Block
Trans-North China Orogen
Eastern Block
35°N
Xi'An
N
400 km
(b)
N
110°E
Yinshan Block
100 km
Guyang
Wuchuan
Alashan
Daqingshan
Wulashan
Jining
Fig. 1c
Khondalite Belt
Datong
40°N
Qianlishan
Ordos Block
Helanshan
High grade TTG gneisses and granulites
Low grade TTG gneisses and greenstones
Paleoproterozoic granulites and khondalites
Trans-North China Orogen
(c)
Yinshan Block
112°E
113°E
114°E
Wuchuan
Sanchakou
Jining
41°N
J1544
Zhuozi
Huhhot
Xiaoshizi
J1448
Tuguiwula
Xinghe
(2)
(1)
J1542
Hongshaba
Xuwujia
Huaian
Khondalite Belt
(6)
Hongsigou
(3)
(5)
Liangcheng
Xumayao
Fengzhen
Heling'er
N
Zhaojiayao
(4)
50 km
Datong
Yangyuan
40°N
Trans-North China Orogen
Quartzo-feldspathic granulites and charnockites
Amphibolite facies metasupracrustal rocks
Granulite facies metasedimentary rocks
Metagabbros and metanorites
Sapphirine-present/absent UHT metapelite localities
S-type granites
Fault
Sample localities
TTG gneisses

Figure 1

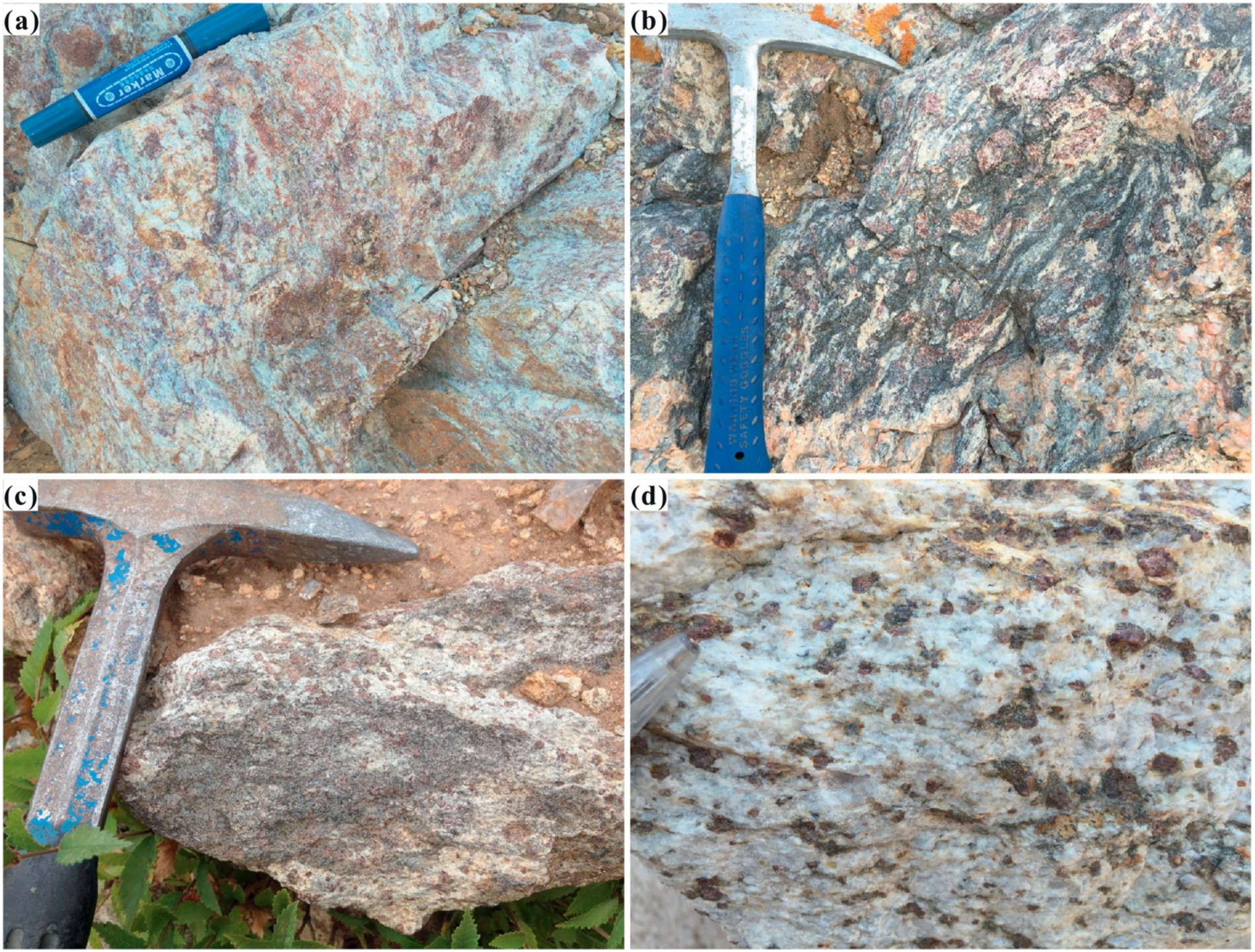

Figure 2

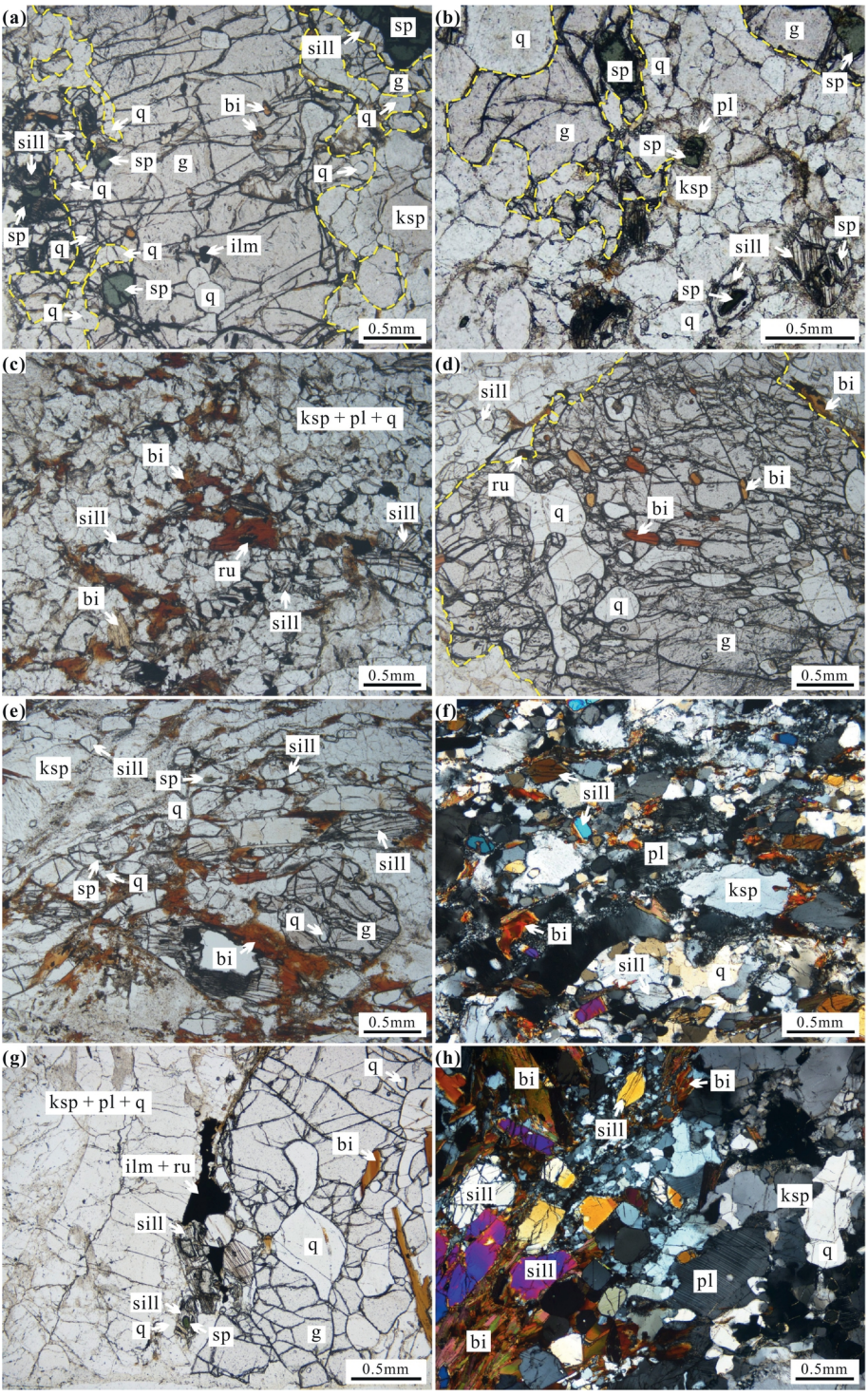
(a)
sp
sill
g
bi
q
q
sill
sp
g
q
q
ksp
sp
q
q
ilm
sp
q
q
0.5mm
(b)
q
g
sp
q
sp
pl
g
sp
ksp
sp
sill
sp
q
0.5mm
(c)
ksp + pl + q
bi
sill
sill
ru
bi
sill
0.5mm
(d)
sill
bi
ru
bi
q
bi
q
g
0.5mm
(e)
sill
ksp
sill
sp
q
sill
sp
q
q
g
bi
0.5mm
(f)
sill
pl
ksp
bi
sill
q
0.5mm
(g)
q
ksp + pl + q
bi
ilm + ru
sill
q
sill
q
sp
g
0.5mm
(h)
bi
bi
sill
sill
ksp
q
sill
pl
bi
0.5mm

Figure 3

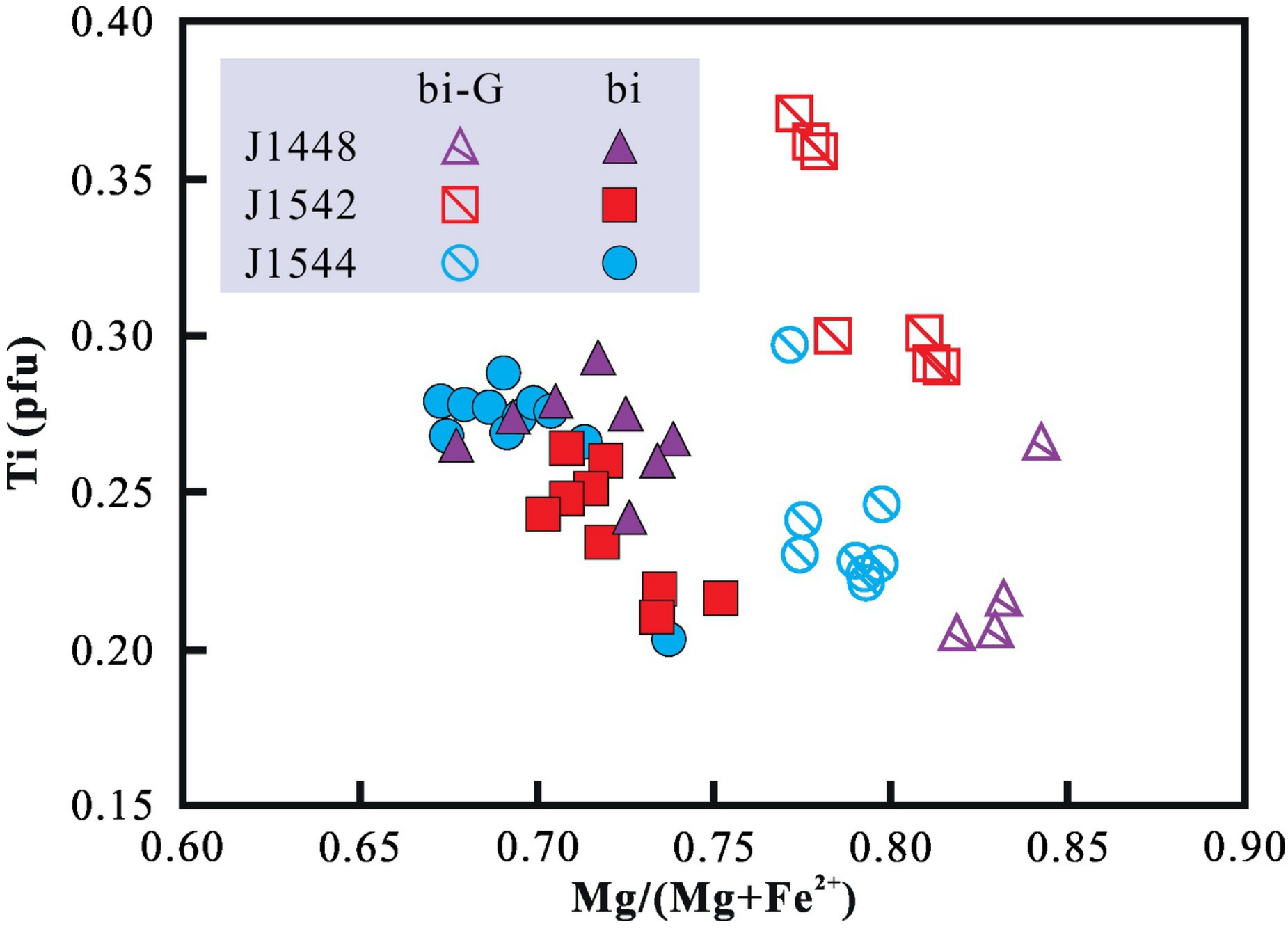
bi-G
bi
J1448
J1542
J1544
0.40
0.35
0.30
0.25
0.20
0.15
Ti (pfu)
0.60
0.65
0.70
0.75
0.80
0.85
0.90
Mg/(Mg+Fe2+)

Figure 4

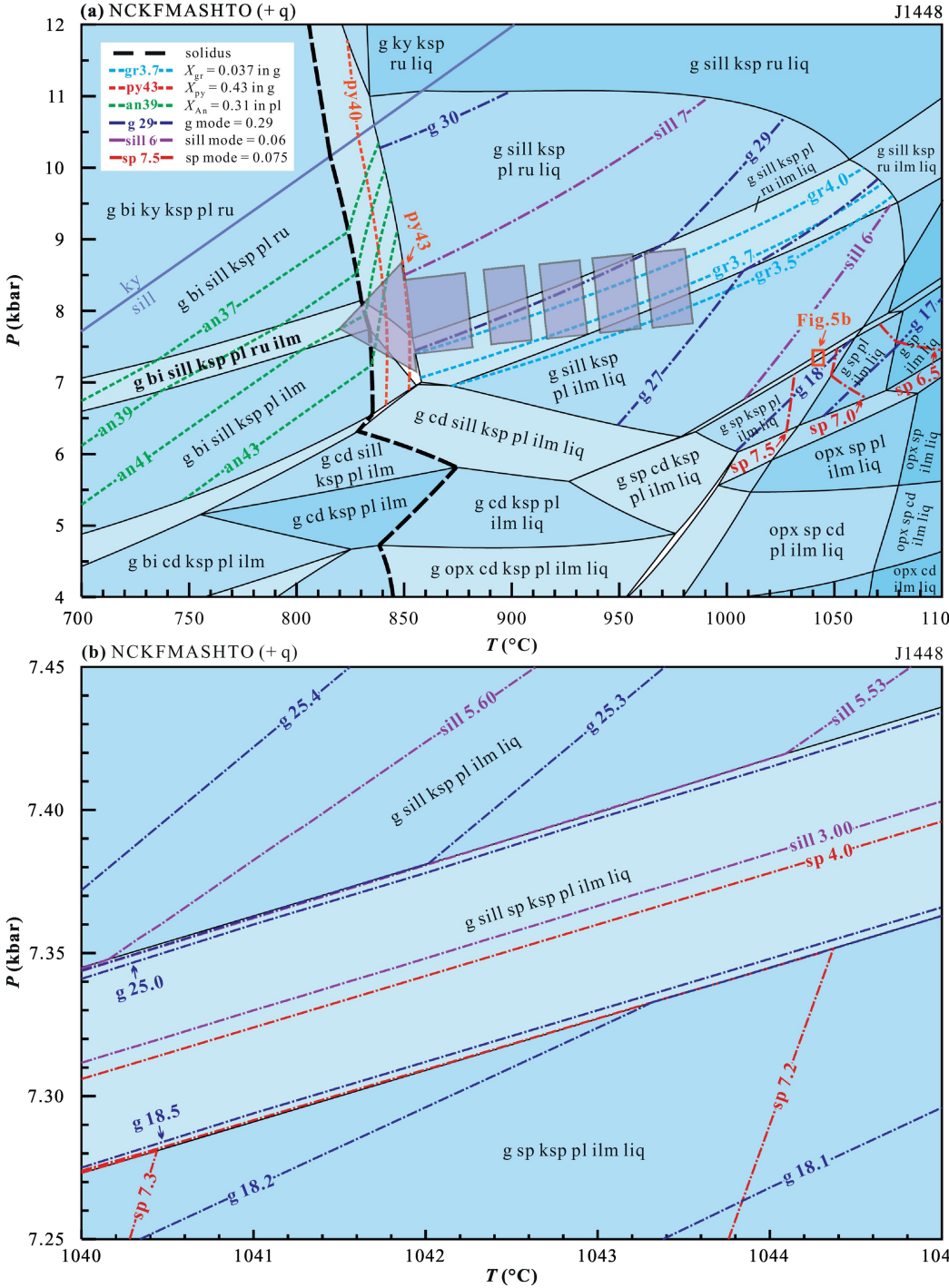
(a) NCKFMASHTO (+ q)
J1448
solidus
gr3.7 X_{gr} = 0.037 in g
py43 X_{py} = 0.43 in g
an39 X_{An} = 0.31 in pl
g 29 g mode = 0.29
sill 6 sill mode = 0.06
sp 7.5 sp mode = 0.075
g ky ksp ru liq
g sill ksp ru liq
g sill ksp pl ru liq
g bi ky ksp pl ru
g bi sill ksp pl ru
g bi sill ksp pl ru ilm
g bi sill ksp pl ilm
g cd sill ksp pl ilm liq
g cd sill ksp pl ilm
g cd ksp pl ilm
g cd ksp pl ilm liq
g sp cd ksp pl ilm liq
g bi cd ksp pl ilm
g opx cd ksp pl ilm liq
opx sp pl ilm liq
opx sp cd pl ilm liq
g sill ksp pl ilm liq
g sp ksp pl ilm liq
g sp pl ilm liq
g sill ksp ru ilm liq
g sill ksp pl ru ilm liq
opx sp ilm liq
opx sp cd ilm liq
opx cd ilm liq
ky
sill
g 30
g 29
sill 7
gr4.0
gr3.7
gr3.5
sill 6
g 17
g 16
sp 6.5
Fig.5b
g 18
sp 7.0
sp 7.5
g 27
py40
py43
an37
an39
an41
an43
P (kbar)
T (°C)
(b) NCKFMASHTO (+ q)
J1448
g 25.4
sill 5.60
g 25.3
sill 5.53
g sill ksp pl ilm liq
sill 3.00
sp 4.0
g sill sp ksp pl ilm liq
g 25.0
g 18.5
sp 7.3
g 18.2
sp 7.2
g 18.1
g sp ksp pl ilm liq
P (kbar)
T (°C)

Figure 5

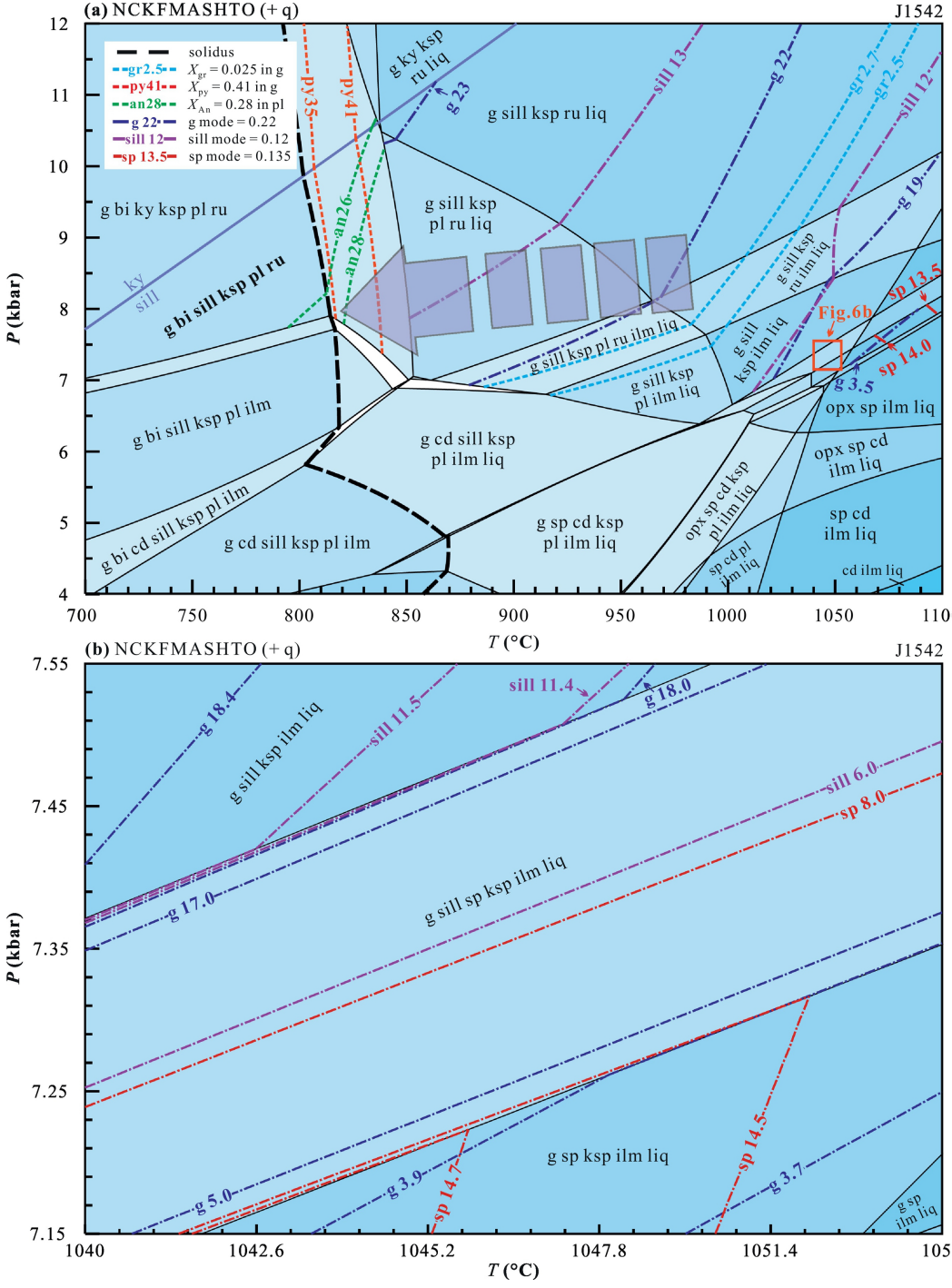
(a) NCKFMASHTO (+ q)
J1542
solidus
gr2.5 X_{gr} = 0.025 in g
py41 X_{py} = 0.41 in g
an28 X_{An} = 0.28 in pl
g 22 g mode = 0.22
sill 12 sill mode = 0.12
sp 13.5 sp mode = 0.135
g bi ky ksp pl ru
g ky ksp ru liq
g 23
g sill ksp ru liq
sill 13
g 22
gr2.7
gr2.5
sill 12
g 19
py35
py41
an26
an28
ky
sill
g bi sill ksp pl ru
g sill ksp pl ru liq
g sill ksp ru ilm liq
sp 13.5
Fig.6b
sp 14.0
g 3.5
g sill ksp pl ru ilm liq
g sill ksp ilm liq
g sill ksp pl ilm liq
opx sp ilm liq
g bi sill ksp pl ilm
g cd sill ksp pl ilm liq
opx sp cd ilm liq
g bi cd sill ksp pl ilm
g cd sill ksp pl ilm
g sp cd ksp pl ilm liq
opx sp cd ksp pl ilm liq
sp cd ilm liq
sp cd pl ilm liq
cd ilm liq
P (kbar)
T (°C)
12
11
10
9
8
7
6
5
4
700
750
800
850
900
950
1000
1050
1100
(b) NCKFMASHTO (+ q)
J1542
g 18.4
g sill ksp ilm liq
sill 11.5
sill 11.4
g 18.0
sill 6.0
sp 8.0
g 17.0
g sill sp ksp ilm liq
g 5.0
g 3.9
sp 14.7
g sp ksp ilm liq
sp 14.5
g 3.7
g sp ilm liq
P (kbar)
T (°C)
7.55
7.45
7.35
7.25
7.15
1040
1042.6
1045.2
1047.8
1051.4
1053

Figure 6

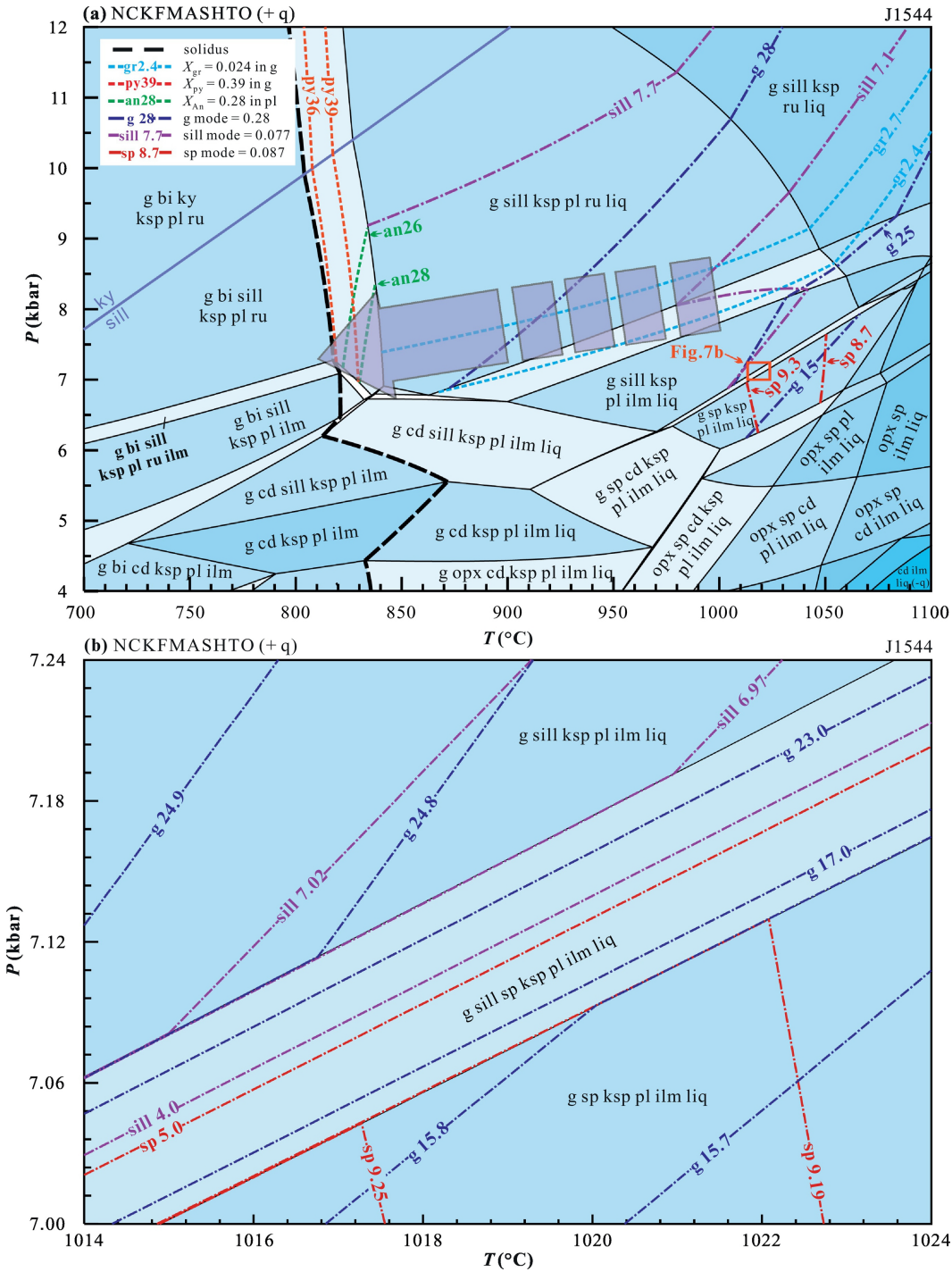
(a) NCKFMASHTO (+ q)
J1544
solidus
gr2.4 X_{gr} = 0.024 in g
py39 X_{py} = 0.39 in g
an28 X_{An} = 0.28 in pl
g 28 g mode = 0.28
sill 7.7 sill mode = 0.077
sp 8.7 sp mode = 0.087
g bi ky ksp pl ru
g bi sill ksp pl ru
g sill ksp pl ru liq
g bi sill ksp pl ilm
g bi sill ksp pl ru ilm
g cd sill ksp pl ilm liq
g cd sill ksp pl ilm
g cd ksp pl ilm
g cd ksp pl ilm liq
g bi cd ksp pl ilm
g opx cd ksp pl ilm liq
g sill ksp pl ilm liq
g sp ksp pl ilm liq
g sp cd ksp pl ilm liq
opx sp cd ksp pl ilm liq
opx sp pl ilm liq
opx sp ilm liq
opx sp cd pl ilm liq
opx sp cd ilm liq
cd ilm liq (sp)
g sill ksp ru liq
ky
sill
an26
an28
py36
py39
sill 7.7
g 28
sill 7.1
gr2.7
gr2.4
g 25
Fig.7b
sp 9.3
g 15
sp 8.7
P (kbar)
T (°C)
(b) NCKFMASHTO (+ q)
J1544
g sill ksp pl ilm liq
g sill sp ksp pl ilm liq
g sp ksp pl ilm liq
g 24.9
g 24.8
sill 6.97
g 23.0
sill 7.02
g 17.0
sill 4.0
sp 5.0
g 15.8
sp 9.25
g 15.7
sp 9.19
P (kbar)
T (°C)

Figure 7

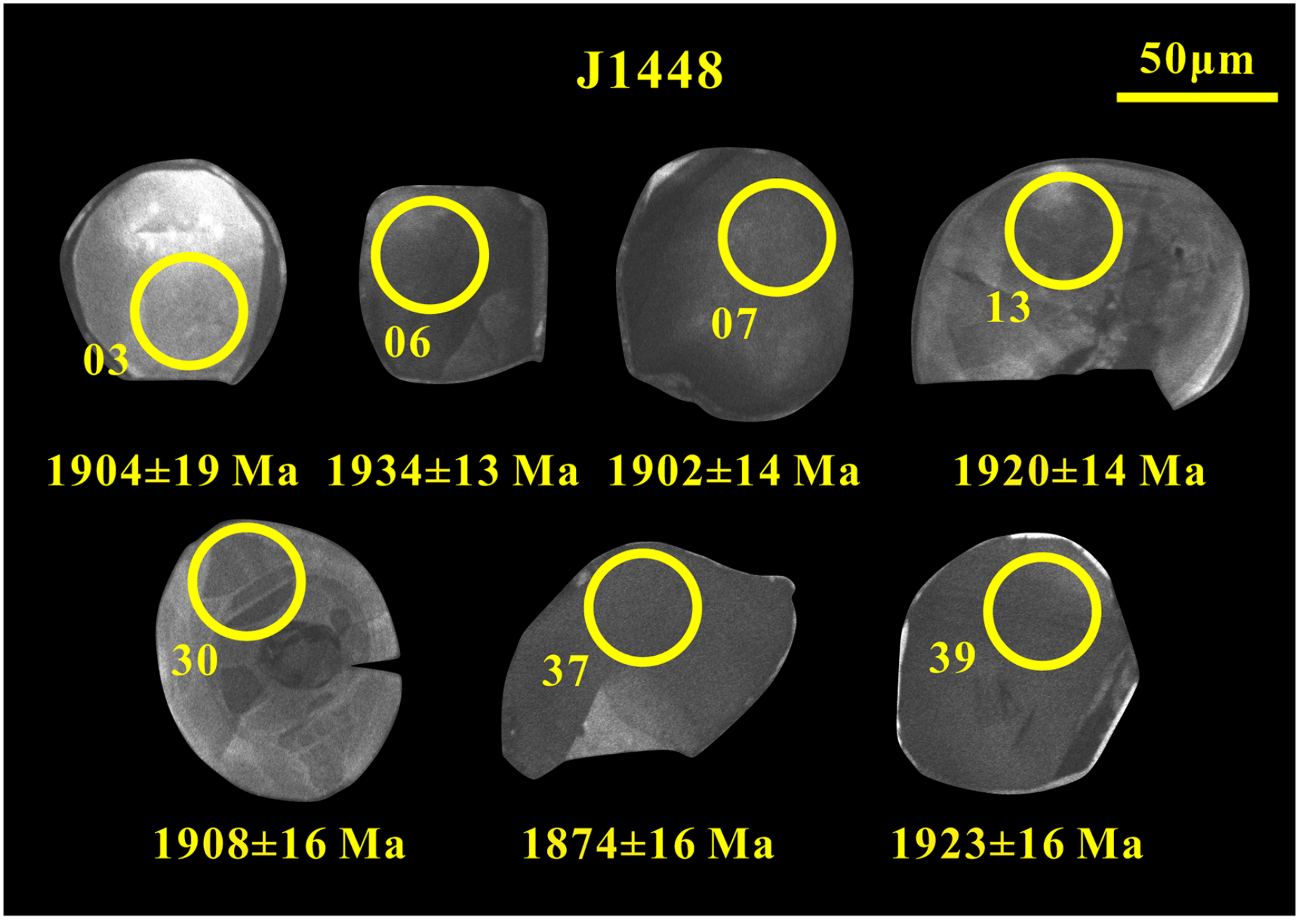
J1448
50µm
03
06
07
13
1904±19 Ma
1934±13 Ma
1902±14 Ma
1920±14 Ma
30
37
39
1908±16 Ma
1874±16 Ma
1923±16 Ma

Figure 8

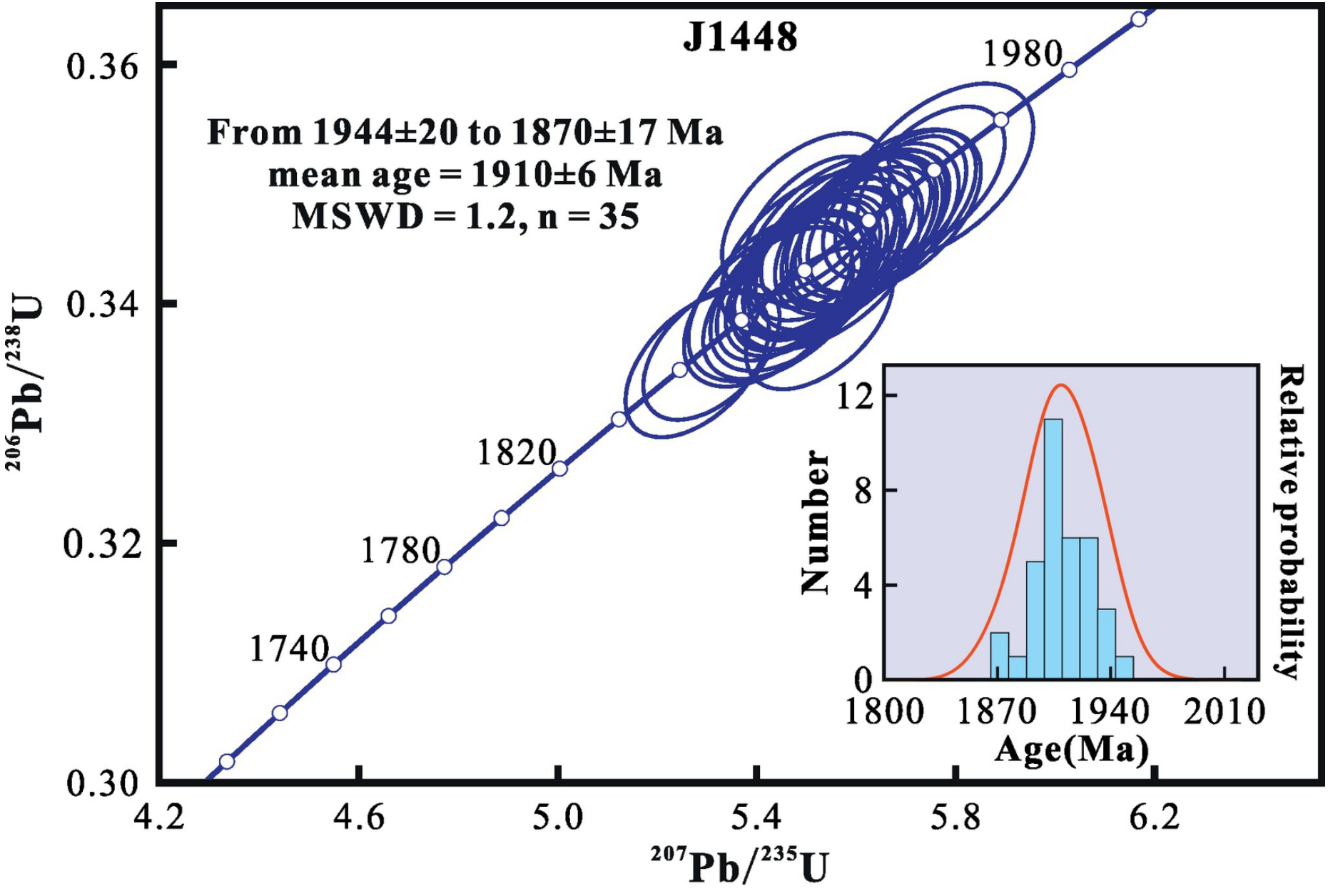
J1448
From 1944±20 to 1870±17 Ma
mean age = 1910±6 Ma
MSWD = 1.2, n = 35
1980
1820
1780
1740
0.36
0.34
0.32
0.30
4.2
4.6
5.0
5.4
5.8
6.2
$^{206}Pb/^{238}U$
$^{207}Pb/^{235}U$
Number
Relative probability
12
8
4
0
1800
1870
1940
2010
Age(Ma)

Figure 9

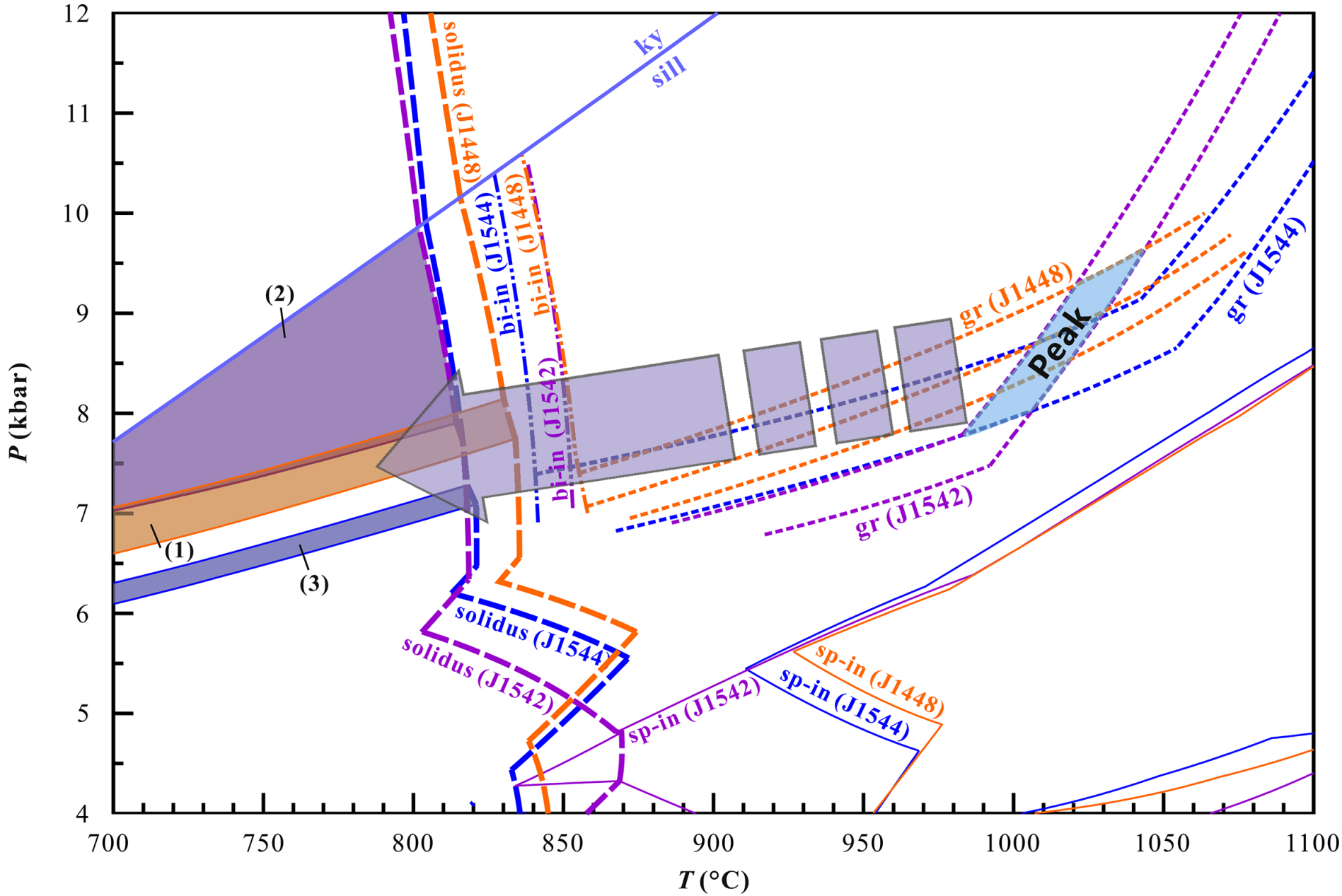
12
11
10
9
8
7
6
5
4
P (kbar)
700
750
800
850
900
950
1000
1050
1100
T (°C)
ky
sill
solidus (J1448)
bi-in (J1544)
bi-in (J1448)
bi-in (J1542)
gr (J1448)
gr (J1544)
gr (J1542)
Peak
(1)
(2)
(3)
solidus (J1544)
solidus (J1542)
sp-in (J1542)
sp-in (J1448)
sp-in (J1544)

Figure 10

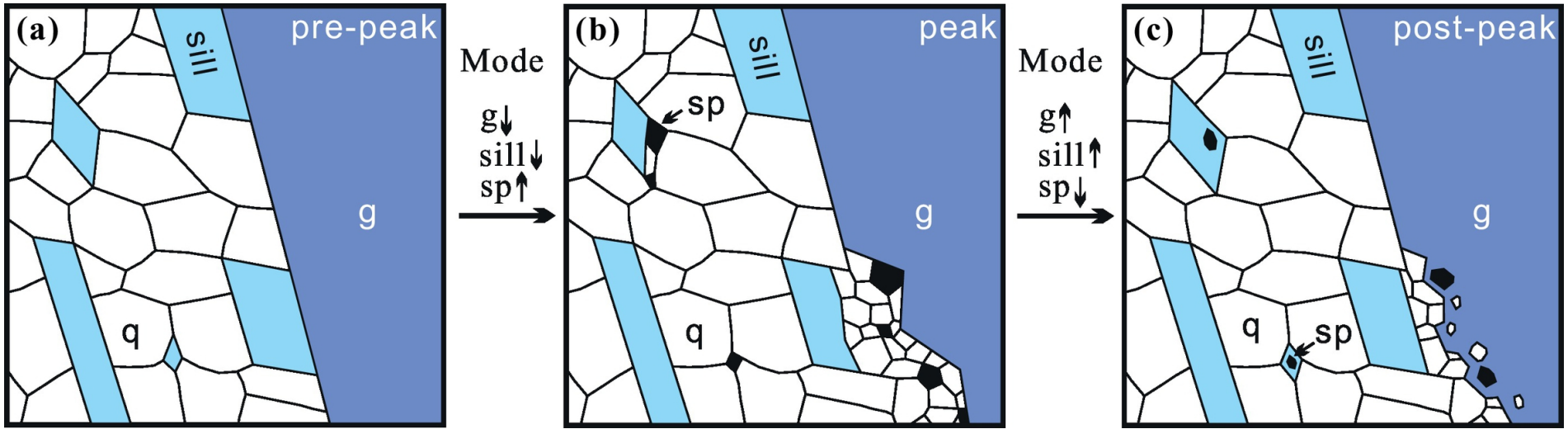
(a)
sill
pre-peak
g
q
Mode
g↓
sill↓
sp↑
(b)
sill
peak
sp
g
q
Mode
g↑
sill↑
sp↓
(c)
sill
post-peak
g
q
sp

Figure 11

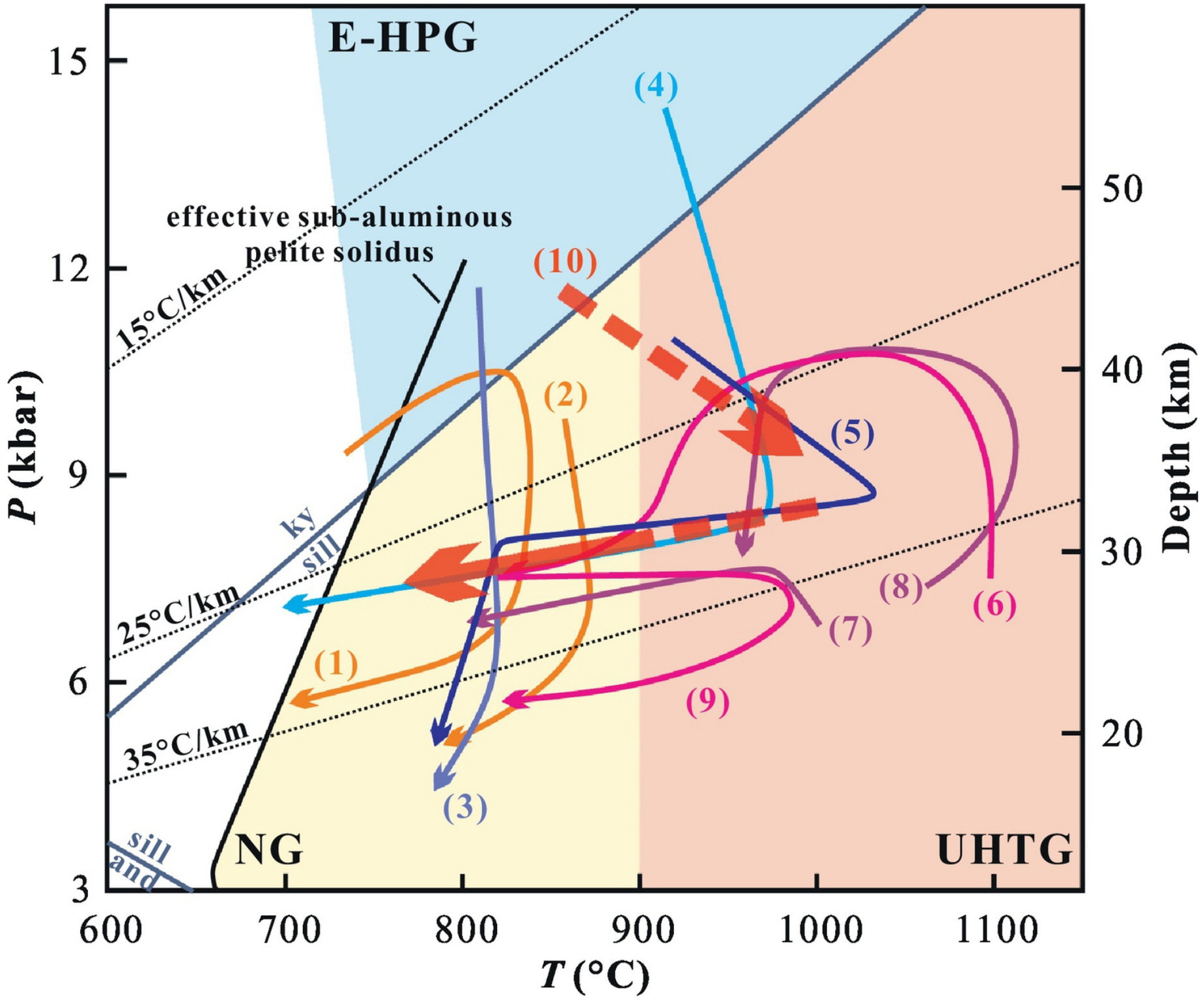
E-HPG
NG
UHTG
effective sub-aluminous
pelite solidus
15°C/km
25°C/km
35°C/km
ky
sill
sill
and
(1)
(2)
(3)
(4)
(5)
(6)
(7)
(8)
(9)
(10)
P (kbar)
T (°C)
Depth (km)
15
12
9
6
3
600
700
800
900
1000
1100
50
40
30
20

Figure 12